

# Observation of CNO solar neutrinos with the Borexino Experiment

von  
APEKSHA SINGHAL

MASTER ARBEIT IN PHYSIK  
vorgelegt der  
FAKULTÄT FÜR MATHEMATIK, INFORMATIK UND  
NATURWISSENSCHAFTEN  
der  
RWTH AACHEN

im November 2020

angefertigt im  
PHYSIKALISCHEN INSTITUT III. B

Erstgutachter und Betreuer

PROF. DR. LIVIA LUDHOVA  
Physikalisches Institut III. B  
RWTH Aachen

Zweitgutachter

PROF. DR. ACHIM STAHL  
Physikalisches Institut III. B  
RWTH Aachen

Ich versichere, dass ich die Arbeit selbstständig verfasst und keine anderen als die angegebenen Quellen und Hilfsmittel benutzt sowie Zitate kenntlich gemacht habe.

Aachen, den

## Abstract

The neutrinos emitted from thermonuclear reactions in the Sun help to unravel the processes occurring in its core. According to the Standard Solar Model predictions, the two processes:  $pp$  (proton-proton) chain and CNO (carbon-nitrogen-oxygen) cycle reactions power the Sun. The  $pp$ -chain processes are the primary source of solar energy while the CNO cycle is hypothesized to be the dominant energy production process in heavier stars and is assumed to contribute less than 1% to the solar energy. This makes it difficult to detect the CNO neutrinos coming from the Sun. All  $pp$ -chain neutrinos have already been detected before. The observation of solar neutrinos from CNO cycle will give a complete picture about the sources of energy in the Sun and will also provide an insight into the longstanding problem of the metallicity of the Sun.

The Borexino Detector, an ultra-pure liquid scintillator located at the Laboratori Nazionali del Gran Sasso, Italy has detected the neutrinos from CNO cycle in the Sun for the first time in history. The challenges faced in the analysis of CNO neutrinos are the low rate of CNO neutrinos and degeneracy of spectral shape of CNO neutrinos to that of  $^{210}\text{Bi}$  background and  $pep$  solar neutrinos. This thesis describes the analysis methods used to extract the different backgrounds and CNO neutrino signal and evaluate systematic uncertainties associated to it. My work concentrates towards optimisation of Monte Carlo simulation in order to prepare simulated  $^{210}\text{Po}$  data specifically used for CNO analysis and determination of constraints like  $^{11}\text{C}$  shift and  $^{210}\text{Bi}$  constraint parameters such as beta leakage and efficiency of MLP discrimination method on  $^{210}\text{Po}$  data. In addition to this, the fit method used to disentangle CNO neutrino signal from backgrounds in data and some of its systematics evaluation is also presented. The main result of the analysis is the exclusion of the absence of CNO solar neutrinos at the significance level greater than  $5.0\sigma$  at 99% confidence level.

# Contents

<b>1</b>	<b>Introduction to Solar Neutrinos</b>	<b>1</b>
1.1	Processes powering the Sun . . . . .	1
1.2	Standard Solar Model . . . . .	5
1.3	Solar neutrino experiments . . . . .	5
<b>2</b>	<b>The Borexino Experiment</b>	<b>10</b>
2.1	Detector Design . . . . .	10
2.2	Detection Principle . . . . .	12
2.3	Backgrounds . . . . .	13
2.4	Data Acquisition . . . . .	15
<b>3</b>	<b>Monte Carlo Simulation of the Detector</b>	<b>19</b>
3.1	Introduction to simulation code . . . . .	19
3.2	Tuning and Validation of MC code . . . . .	20
3.3	Construction of MC PDFs . . . . .	21
3.4	Normalisation of $^{210}\text{Po}$ PDFs and Study of triggering inefficiency . . . . .	22
<b>4</b>	<b>Analysis Strategy: Data Selection and Constraints</b>	<b>30</b>
4.1	Data Selection . . . . .	30
4.1.1	Three Fold Coincidence (TFC) cut . . . . .	31
4.2	Constraints . . . . .	36
4.2.1	$pep-\nu$ constraint . . . . .	36
4.2.2	Upper limit on $^{210}\text{Bi}$ . . . . .	37
<b>5</b>	<b>Multivariate Monte Carlo Fit of Data</b>	<b>48</b>
5.1	Fitting Method . . . . .	48
5.2	Fit Results of Phase 3 Data . . . . .	49
<b>6</b>	<b>Final Result with systematics</b>	<b>53</b>
6.1	Systematics related to Fitting Method . . . . .	53
6.2	Other Sources of Systematics . . . . .	53
6.3	Final Results . . . . .	54
6.4	Counting Analysis . . . . .	55
<b>7</b>	<b>Conclusion and Outlook</b>	<b>57</b>
<b>8</b>	<b>Publications</b>	<b>59</b>

# Chapter 1

## Introduction to Solar Neutrinos

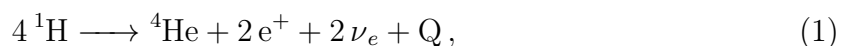
This chapter describes the fusion processes occurring in the core of the Sun and classifying the neutrinos coming from these processes which are referred to as solar neutrinos. In section 1.1, the two chains of processes fueling the Sun are discussed which are called *pp* chain and CNO cycle. The importance of studying solar neutrinos is also cited in this section.

Section 1.2 illustrates about the theoretical models, known as Standard Solar Models (SSMs) which rely on the information coming from other measurements to predict the neutrino flux from the Sun. This in turn helps to determine the picture of the Sun's core.

Section 1.3 classifies the different solar neutrino experiments based on their detection methods. Various important historical solar neutrino experiments are also described and their results are stated in this section.

### 1.1 Processes powering the Sun

As stated in [1] and [2], the stars like Sun are powered through various thermonuclear reactions occurring in its core. The energy is generated in the Sun through the following reaction:



where  $Q$  denotes the  $Q$ -value of the reaction, i.e the energy released during the nuclear process. The value of  $Q$  is 26.73 MeV. Here, a single helium nucleus is formed due to fusion of four hydrogen nuclei and results in the emission of two positrons, two electron neutrinos, and the energy. This reaction is based on the findings of F.W. Aston. He discovered that the mass of helium nucleus is less than the combined masses of four hydrogen nuclei. This mass difference leads to difference in the binding energy of reactant and product nuclei of the reaction and therefore results in the emission of energy. Hence, this process can allow our star to shine.

The formation of He nucleus as an end product in equation 1 takes place through different sequences of nuclear reactions. Theoretical models (described in sec 1.2) predict that the two chains of reactions named as *pp*-chain and CNO-cycle are responsible for fueling the stars like Sun. The relative contribution of the two channels depend on temperature of the core of the star (Fig 1.1). In Sun, *pp*-chain reactions are the dominant mechanisms and contribute  $\sim 99\%$  to the solar luminosity. And the remaining  $\sim 1\%$  contribution to the energy of the sun is thought to be accounted by the reactions in CNO-cycle. However the

CNO cycle, a subdominant cycle in Sun, is believed to be the primary source of energy in stars with mass greater than about 1.3 times the solar mass.

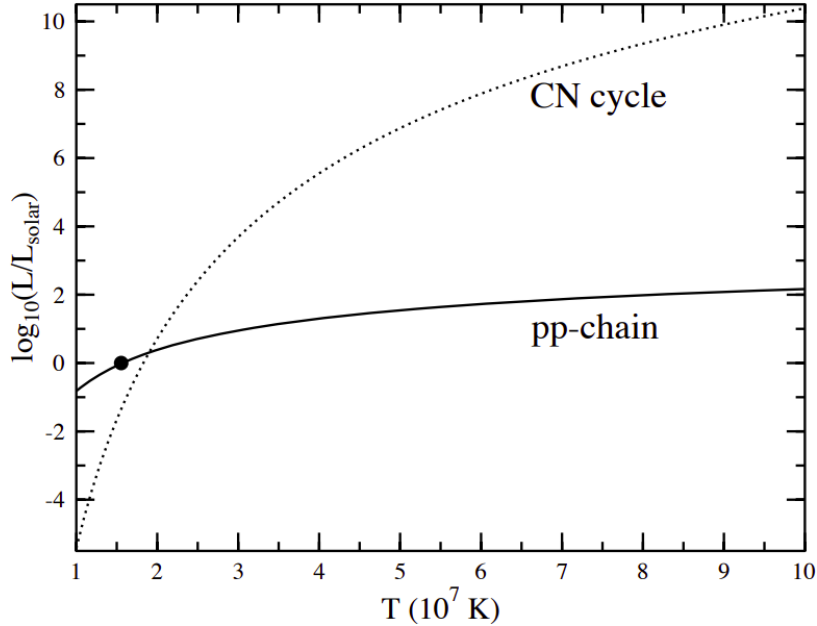


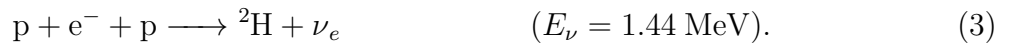
**Figure 1.1:** CNO and  $pp$ -cycle as function of temperature of star's core. The black circle denotes the Sun [3].

## $pp$ -chain

The first step in the  $pp$ -chain reaction is the fusion of two protons to form deuterium with branching ratio of  $\sim 99.6\%$  :



The alternative  $pep$  reaction accounts for the remaining  $\sim 0.4\%$  branching ratio. In this case, mono-energetic neutrinos ( $pep \nu_s$ ) are released :



Further the chain proceeds with proton absorption by deuterium, produced in one of the previous reactions, with no emission of neutrinos but release of energy of 5.49 MeV occurs through gamma photons:



After this step, the chain is now divided into three terminations named as  $pp$ -I,  $pp$ -II and  $pp$ -III reactions. Among these three reactions,  $pp$ -I has the highest probability of 85% to occur with Q-value = 12.86 MeV:



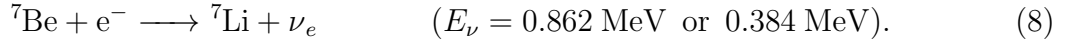
Furthermore,  ${}^4\text{He}$  can also be created using the so-called *hep* reaction and hence the highly energetic neutrinos emitted in this reaction are called as *hep- $\nu$ s*. They have not been observed yet due to their very low rate of production, since this reaction has extremely low probability ( $\sim 10^{-5}\%$ ) to occur:



The termination reactions, *pp*-II and *pp*-III, are preceded by a reaction forming  ${}^7\text{Be}$ . This reaction accounts for remaining  $\sim 15\%$  of probability and has a Q-value of 1.59 MeV:



Formation of  ${}^7\text{Be}$  leads to 2 branches of reactions. The first reaction is the electron capture by  ${}^7\text{Be}$  emitting mono-energetic neutrinos and creation of  ${}^7\text{Li}$ . Depending on whether  ${}^7\text{Li}$  is produced in ground state or excited state, the energy of neutrinos is either 0.862 MeV or 0.384 MeV.



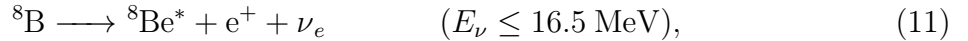
This *pp*-II branch is ended via the following reaction:



The alternative branch starts with the creation of  ${}^8\text{B}$  :



Now, the  ${}^8\text{B}$  decays via emitting neutrino with continuous spectrum and the product  ${}^8\text{Be}$  undergoes  $\alpha$  decay ending the *pp*-III branch reaction :



## CNO-cycle

The CNO cycle, suggested by C.F. von Weizsäcker [4], consists of reactions where four protons are burned to form  ${}^4\text{He}$  catalysed by  ${}^{12}\text{C}$ ,  ${}^{14}\text{N}$ , and  ${}^{16}\text{O}$  nuclei. This reaction mechanism involves 2 subcycles as shown in Fig 1.2. The dominant one is subcycle-I with the probability of 99.95% to occur and the secondary cycle, CNO subcycle-II accounts for remaining 0.05% probability.

The subcycle-I starts with proton capture by  ${}^{12}\text{C}$  to form  ${}^{13}\text{N}$  and proceeds as following:



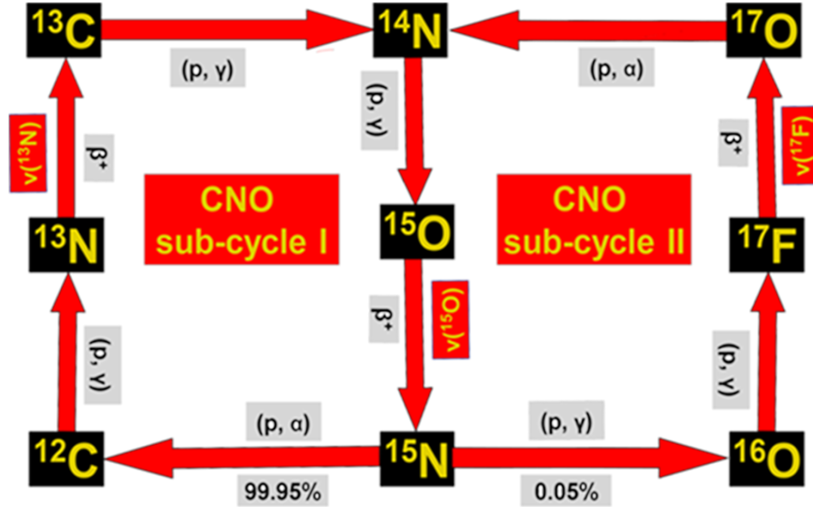


Figure 1.2: The 2 subcycles of the CNO reaction chain



At this stage,  ${}^{15}\text{N}$  either forms back to  ${}^{12}\text{C}$  as following:



or is converted to  ${}^{16}\text{O}$  and further proceeds as below to form subcycle-II:



Now, the reaction 16 is repeated and the cycle continues as before.

The expected energy spectra of the solar neutrinos produced in all the previously mentioned reactions is shown in Fig 1.3. Here, the unit of flux is  $\text{cm}^{-2}\text{s}^{-1}\text{MeV}^{-1}$  for continuous spectra and  $\text{cm}^{-2}\text{s}^{-1}$  for mono-energetic ones.

The study of solar neutrinos is important because they act as probe to gain information about energy loss or production mechanism in the Sun. The advantage of studying neutrino luminosity over optical luminosity is that since neutrinos are weakly interacting particles, they promptly escape from core of the Sun. However, it takes around  $10^5$  years for photons to escape the Sun's core.

In addition to this, the study of especially CNO solar neutrinos will help to solve a puzzle known as "metallicity problem" which is discussed in the next section in more detail.

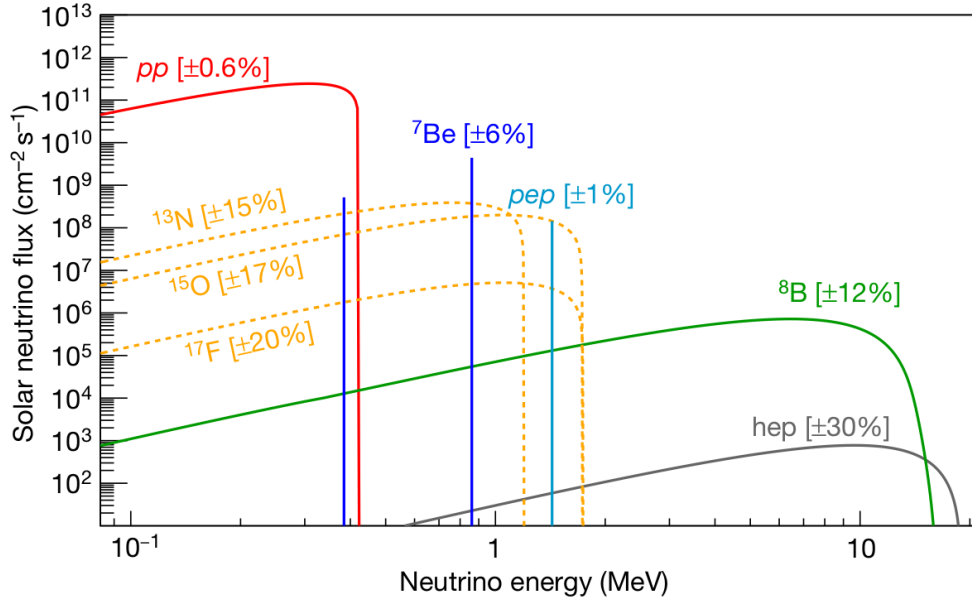


Figure 1.3: Theoretical energy spectrum of different solar neutrinos [5].

## 1.2 Standard Solar Model

Standard Solar Models (SSMs) [6] are the quantitative descriptions of evolution of star of one solar mass. Its parameters are calibrated such that it matches the surface properties of the sun at present. The elemental abundances, derived from the spectroscopic data from the Sun, are the main constraints used in its construction. It is derived from conservation laws and energy transport equations and various input parameters like present day solar luminosity, radius, mass, age, radiation opacity, nuclear cross sections,  $Z/X$  ratio (metallicity) and equation of state. Then, these models help to predict the neutrino fluxes and speed profiles of sound waves (helioseismology).

The  $Z/X$  ratio or metallicity refers to the fraction of elements heavier than He. Heavy-element abundances from GS98 (Grevesse and Sauval 1998) forms a model which has been found in good agreement with the helioseismological data. This is known as older high-metallicity scenario ( $Z/X = 0.0229$ ).

However, the development of 3-D hydrodynamic models of solar atmosphere since 2001, has led to significant decrease in the value of  $Z/X$  ratio to 0.0178. Low element abundance from AGSS09 fails to match the helioseismic probes of solar properties. This is known as newer low-metallicity scenario. And this discrepancy is known as "solar abundance problem".

The solution of this problem lies in the solar neutrino measurement, especially the observation CNO neutrinos and the measurement of its flux. Since this flux predicted by high metallicity SSM differs significantly ( $\sim 28\%$ ) from that of low metallicity SSM, comparison of the measurement with the predictions could contribute to the solution of this problem.

## 1.3 Solar neutrino experiments

As already stated, the neutrinos are so unreactive that they immediately escape from sun's core to space unlike the photons. However, this also means that they are difficult to

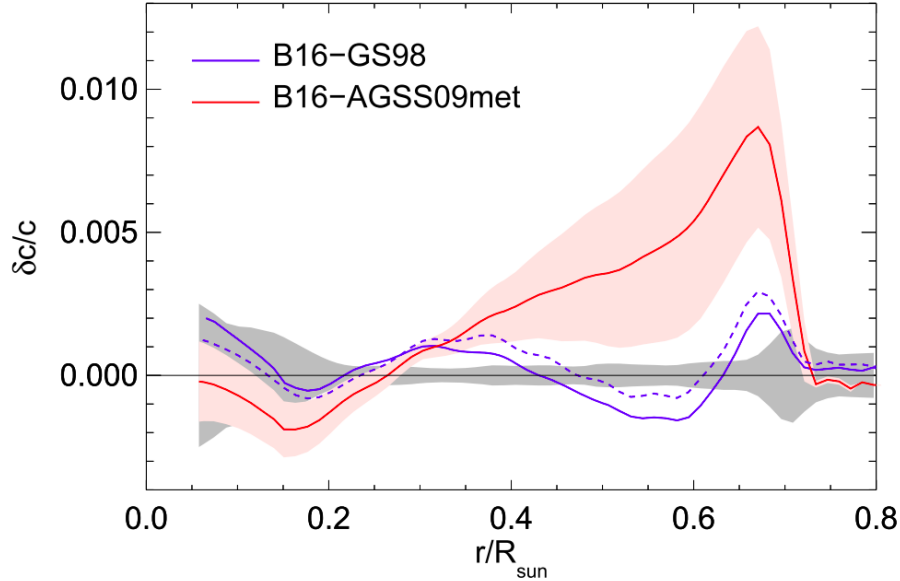


**Figure 1.4:** The fractional difference of sound speed between data and model. Blue line shows the high metallicity scenario while red line shows low metallicity scenario [6].

capture or detect due to their small interaction cross-section. In order to overcome this obstacle, several giant neutrino detectors have been proposed and built over a long period of time. Many efforts have been made to reduce the sources of background to make the neutrino detection precise as much as possible. These detectors make use of detection of the secondary particles created when neutrinos interact with the target. The experiments have been mainly classified based on their detection techniques.

In principle, there are two categories of solar neutrino experiments:

- **Radiochemical experiments** - The principle of detection in the radiochemical experiments is the detection of the decay products of the unstable daughter nuclei in the following charged current interaction:



This technique is only sensitive to electron neutrinos at MeV energies since muons and tau leptons would be heavy to get created. As the detection is based on the counting of daughter nuclei, this method measure the integral flux above a certain energy threshold. This threshold varies for different experiments as shown later.

- **Real time experiments** - These kind of experiments exploit typically elastic scattering (in liquid scintillator detectors) and water Cherenkov radiation processes (in Cherenkov detectors) to detect neutrinos. However, some experiments like SNO also make use of detection techniques like neutral and charged current interactions which is discussed later. The advantage in these experiments is that the neutrino energy spectrum is measured along with other information like interaction position in the detector including the arrival direction of neutrino in Cherenkov detectors.

## Historical Experiments

### Homestake Experiment

This experiment [7] was built in Homestake gold mine in South Dakota in USA with a tank of perchloroethylene ( $C_2Cl_4$ ) serving as target at 4100 mean water equivalent (m.w.e). This was the first solar neutrino experiment running between 1970-1994. It is the chlorine based experiment using the following decay reaction to detect neutrinos:

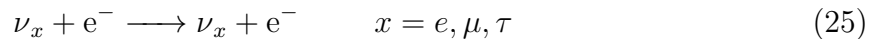


The energy threshold of this reaction is 0.814 MeV. Hence, this experiment could not measure the  $pp$ -neutrino flux. The  $^{37}\text{Ar}$  produced is extracted through helium purging out the tank and is counted in proportional counter via detecting the auger electrons resulting from electron capture of  $^{37}\text{Ar}$ .

The average count rate measured with data of more than 20 years is  $2.56 \pm 0.16(\text{stat}) \pm 0.15(\text{sys.})$  SNU<sup>1</sup>. When compared to the prediction of SSM which is  $9.3 \pm 1.3$  SNU, this gives the sign of neutrino deficit, later widely known as the solar neutrino problem.

### (Super)-Kamiokande

This water Cherenkov detector [8] is situated in the Kamioka mine in Japan at the depth of 2700 m.w.e. This experiment was able to measure  $^8\text{B}$  solar neutrinos in real time via neutrino-electron scattering :



This scattering process is sensitive to all active neutrinos but cross section for scattering by  $\nu_e$  is larger than that of  $\nu_\mu$  and  $\nu_\tau$ . The scattered electron emits the Cherenkov light having the energy threshold of 5 MeV and in turn, the light is collected by the several PMTs located on the tank surface of the detector. This technique has made solar neutrino to disentangle from backgrounds as there is strong directional dependence of scattered electron to arrival direction of the neutrino. The measurement of 1496 days has yielded the time averaged flux of  $^8\text{B}$  neutrinos =  $2.35 \pm 0.02(\text{stat}) \pm 0.08(\text{sys}) \cdot 10^6 \text{ cm}^{-2} \text{ s}^{-1}$  [9]. This corresponds to only 46.5% of SSM prediction. Hence, this confirms the results of chlorine based experiment.

### Gallium Experiments

The gallium based experiments built so far are GALLEX/GNO and SAGE. The main principle of the detection is via radiochemical method where  $^{71}\text{Ga}$  serves as target and decay as following:



with the energy threshold of 0.233 MeV. This means that this radiochemical technique could measure low energy solar  $pp$  neutrino flux. The detection is done using proportional counters by detecting Auger electrons resulting from the electron capture reaction of  $^{71}\text{Ge}$ .

GALLEX (gallium experiment) ([10]-[11]) was set up in the Gran Sasso underground laboratory in Italy and took data from 1991 to 1997. It used 30.3 t gallium in the form of  $\text{GaCl}_3$  solution. When equilibrium between the production and decay rates is achieved,  $^{71}\text{Ge}$  is extracted by purging nitrogen and is converted to german gas ( $\text{GeH}_4$ ). Its decay

---

<sup>1</sup>1 SNU =  $10^{-36}$  captures per target atom per second

is observed in proportional counters. GNO experiment [12] is the upgrade of GALLEX experiment running from 1998 till 2003.

The SAGE (Soviet-American Gallium Experiment) [13] was located in the Baksan underground laboratory in Russia. The detection principle is same as for GALLEX/GNO experiment but the difference lies in the usage of metallic gallium as target in SAGE. The combined results of all three experiments is  $66.1 \pm 3.1$  SNU. On comparing with the predictions of SSM, deficit of solar neutrinos is confirmed.

## SNO

The SNO (Sudbury Neutrino Observatory) detector ([14]-[16]) is a water Cherenkov detector. It was located at 6010 m.w.e in Creighton mine near Sudbury, Ontario in Canada. The detector consists of acrylic vessel of 12 m in diameter containing heavy water ( $D_2O$ ). This vessel is immersed in light water ( $H_2O$ ) and is surrounded by 9456 PMTs mounted on geodesic sphere. This principle of detection of  $^8B$  solar neutrinos is through 3 processes:

$$\nu_e + {}^2H \longrightarrow p + p + e^- \quad (CC), \quad (27)$$

$$\nu_x + {}^2H \longrightarrow p + n + \nu_x \quad x = e, \mu, \tau \quad (NC), \quad (28)$$

$$\nu_x + e^- \longrightarrow \nu_x + e^- \quad x = e, \mu, \tau \quad (ES). \quad (29)$$

The charged current interaction (CC) is flavour-dependent process and hence, only electron flavoured neutrinos interact via this process. The energy threshold of this process is 1.44 MeV. The emitted electron is detected through Cherenkov light. The advantage of CC reaction is that it provides spectral measurements. The neutral current interaction (NC) is equally sensitive to neutrinos of all flavours and has energy threshold of 2.2 MeV. In this detection technique, neutron detection is critical and various methods were used in different phases to enhance neutron detection efficiency. Gammas are emitted on neutron capture and in turn, are detected through detection of Compton electrons or  $e^-e^+$  pairs. The elastic scattering (ES), as already described in SuperKamiokande section, is sensitive to all flavors of neutrinos but has more cross section for  $\nu_e$  and provides best directionality measurement.

This experiment has provided strong evidence concerning neutrino oscillation by measuring flux of electron and non-electron component of neutrinos coming from Sun (Fig 1.5). This experiment received the Nobel Prize in 2015 along with SuperKamiokande for the experimental confirmation of neutrino oscillation hypothesis.

In the next chapter, the currently running solar neutrino experiment, Borexino, will be described.

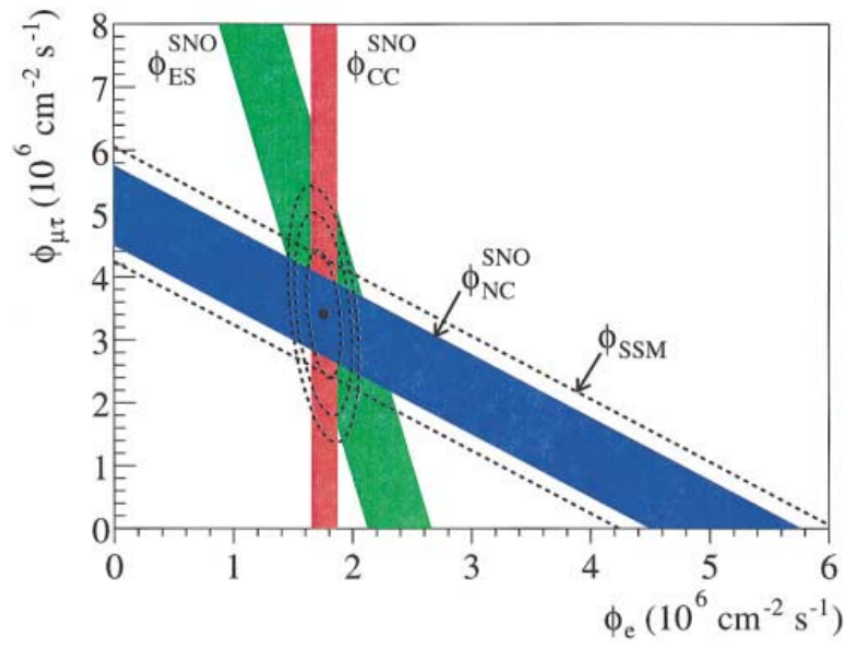


**Figure 1.5:** Flux of non-electron component in solar neutrinos vs flux of electron component as measured by SNO [14].

## Chapter 2

# The Borexino Experiment

This chapter introduces the Borexino experiment including its design and operations. Section 2.1 describes the setup of the Borexino detector in detail focusing on the structure and its different components. The method used in the detector to detect solar neutrinos is presented in section 2.2. In addition to this, the different terms allocated to important time periods of the experiment are explained in this section.

Section 2.3 illustrates all kinds of backgrounds crucial for CNO- $\nu$  analysis. Here, the properties about each isotope which act as background and the method used to estimate its level of contamination is described. Section 2.4 contains the overview of data acquisition systems of the detector. This section introduces the electronics of the detector and data processing software.

### 2.1 Detector Design

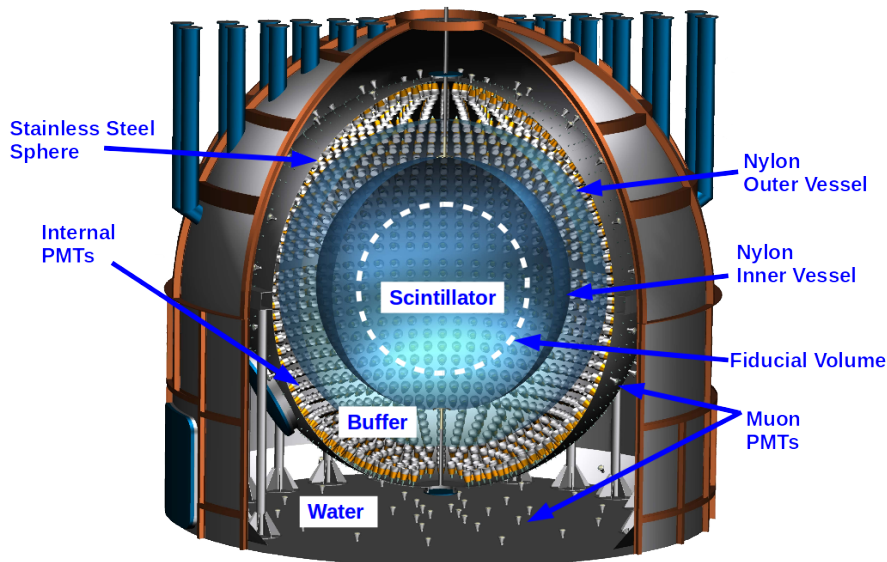


Figure 2.1: The complete set-up of Borexino Detector<sup>1</sup>.

---

<sup>1</sup>Source: Borexino Collaboration

Borexino is a liquid scintillator based detector [17], located in the Hall C of Laboratori Nazionali del Gran Sasso (LNGS) in Italy. Since it is setup in deep underground lab of LNGS at a depth of about 3800 m.w.e, the cosmogenic muon background is highly suppressed by a factor of  $10^6$ . It is designed to achieve extremely low background conditions and provide the largest possible fiducial volume of ultra-clean scintillator. The structure of this detector is such that the radio-purity decreases from center of set of concentric shells to outside of the detector. The layout of the detector is shown in Fig 2.1.

The inner part of the detector consists of Stainless Steel Sphere (SSS) which acts as both container of 278 t of liquid scintillator and mechanical support for PMTs. The radius of SSS is 6.85 m. It contains inner vessel of radius 4.25 m and outer vessel of radius 5.50 m, both being made of nylon and have thickness of 125  $\mu\text{m}$ . The inner vessel (IV) consists of the active medium serving as neutrino target. This active medium is a solution of PPO (2,5- diphenyloxazole) in pseudocumene (PC, 1,2,4-trimethylbenzene) at a concentration of 1.5 g/l. The inner vessel is surrounded by the buffer solution containing PC with small amount (initially 5 g/l) of dimethylphthalate (DMP) which is added as light quencher to further reduce the scintillation yield of pure PC. PC/PPO was chosen as scintillating medium due to its characteristics such as high scintillation yield ( $10^4$  photons/MeV), high light transparency and fast decay time ( $\sim 3$  ns). These features are required to ensure good energy resolution, precise spatial reconstruction and good discrimination between  $\beta$  and  $\alpha$  like events. And the use of PC as buffer is convenient since it matches both density and refractive index of scintillator to reduce buoyancy force for nylon vessel and avoiding optics aberrations spoiling the spatial resolution. Combining the effects of scintillator and buffer leads to the scintillation yield of 500 photo-electrons per MeV or 5% of energy resolution at 1 MeV. The outer vessel (OV), immersed in buffer solution, acts as barrier against  $^{222}\text{Rn}$  originating from external materials like steel, glass and PMTs material.

2212 PMTs that are mounted on the inner surface of SSS, collects the scintillation light from vessel. All except 384 PMTs are equipped with light concentrators which are designed to reject the light not arriving from active scintillator volume. Those remaining 384 PMTs are used to study this background and help in the identification of muons that cross the buffer and not IV.

SSS is enclosed in a large dome shaped tank filled with ultra-pure water. The tank has a cylindrical base of diameter 18 m and hemispherical top with a height of 16.9 m. This is depicted in Fig 2.1. This water tank (WT) act as powerful shielding against neutron and  $\gamma$  rays background emanating from surrounding rocks. Besides this, it is also used as Cherenkov muon counter and tracker. This muon veto imposes an further reduction in muon flux, necessary to meet Borexino radio-purity requirements. WT is equipped with 208 PMTs on outer surface of SSS and floor of the tank, that collects Cherenkov light emitted by muons passing through water. The tracking of through-going muon is useful in the reduction of  $^{14}\text{C}$  background for the CNO analysis. SSS and interior of WT is covered with layer of Tyvek, a white paper-like material made of polyethylene fibres to enhance the light collection efficiency. All the materials of detector internal components discussed so far were selected to ensure extremely low radioactivity.

## 2.2 Detection Principle

In Borexino detector, solar neutrinos are detected by means of elastic scattering of electrons:

$$\nu_x + e^- \longrightarrow \nu_x + e^- \quad x = e, \mu, \tau. \quad (30)$$

In this elastic scattering process, a fraction of neutrino energy  $E_\nu$  is transferred to electron and the interaction of electron with the scintillating medium generates the signal. The energy of electron spectrum ranges from zero to a maximum value of kinetic energy. Therefore, even in case of mono-energetic neutrinos, we have continuous electron recoil spectrum. Using the kinematic relations of the scattering process, the maximum kinetic energy of recoiled electron is given by:

$$T_e^{max} = \frac{E_\nu}{1 + \frac{m_e c^2}{2E_\nu}}, \quad (31)$$

where  $m_e c^2$  is the electron rest energy.

Borexino can detect neutrinos of all flavors but cross section for scattering by  $\nu_e$  is larger than that of  $\nu_\mu$  and  $\nu_\tau$ , because  $\nu_e$  interact through both charged current (CC) and neutral current (NC), while others interact through NC only. The elastic scattering has no intrinsic energy threshold but due to  $^{14}\text{C}$  beta spectrum, the energy threshold is raised to 0.2 MeV. Here, electron recoils induced by different neutrino flavors cannot be distinguished event-by-event. Other drawbacks of this detection technique are that the information about direction of neutrino is lost in liquid scintillator detectors and neutrino induced events can't be distinguished from the events occurring due to  $\beta/\gamma$  radioactivity. The expected rate of neutrino-electron scattering in a given target is calculated as the product of the incoming neutrino flux  $\Phi_\nu$ , number of electrons in the target  $N_e$  (for Borexino, the value is  $(3.307 \pm 0.015) \cdot 10^{31}$  /100 ton) and the neutrino-electron elastic scattering cross section.

## Timeline of the Experiment

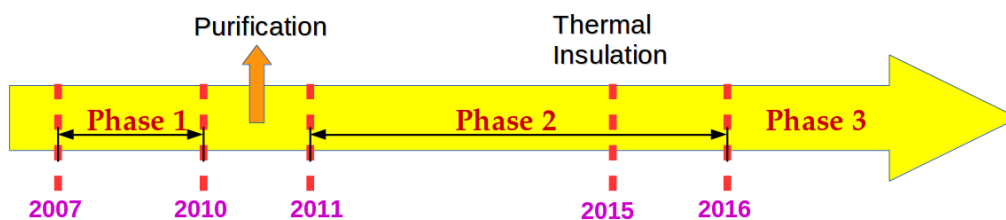


**Figure 2.2:** Figure shows important periods and operations of the experiment

The Borexino Experiment started data taking in May 2007. The period of data taking between 2007 and 2010 is referred to as "Phase 1". "Phase 2" started in December 2011 after an extensive purification campaign and this phase continued till May 2016. Meanwhile, an important operation of "Thermal Insulation" was carried out in 2015 to thermally stabilise the detector which is crucial for CNO analysis. The "Phase 3" began in 2016 and has been ongoing at present.

## 2.3 Backgrounds

As discussed in previous section, the scattering of a neutrino on an electron in Borexino is intrinsically not distinguishable from  $\beta$  radioactivity or from Compton scattering from  $\gamma$  radioactivity. In order to detect solar neutrinos and for their precise measurement, an extreme purity of scintillator and detector material is necessary. To achieve extreme radio-purity of the detector, several measures for purification were taken during installation of detector. A dedicated purification campaign in 2010 - 2011 was done to achieve unprecedented levels of scintillator of radio-purity. However, there are still some relevant backgrounds present which are described below:

### Internal Backgrounds

It refers to the radioactive contaminants present inside the scintillator. Main internal backgrounds are:

#### $^{14}\text{C}$

$^{14}\text{C}$  is produced in the upper atmospheric layers through the reaction:



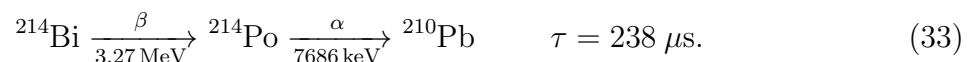
It decays via emitting  $\beta$  particle having end point at 156 keV and has mean life-time of 8270 years. It dominates the low energy part of the spectrum and determines the detector's low energy threshold. Since  $^{14}\text{C}$  is chemically identical to  $^{12}\text{C}$ , which is an intrinsic ingredient of the scintillator, it could not be removed from the detector through purification. However for CNO analysis, the low energy threshold was chosen such that  $^{14}\text{C}$  decays are not taken into account.

#### $^{85}\text{Kr}$

$^{85}\text{Kr}$  ( $\beta$ -emitter, end-point: 0.687 MeV, 15.4 years mean lifetime) is present in the air itself due to nuclear explosions caused by humans. Its spectral shape is similar to the spectrum of  $^7\text{Be}-\nu$ . The purification campaign has led this background to reduce by a factor of 4.6 ([18]-[19]). With low probability,  $^{85}\text{Kr}$  decays to  $^{85\text{m}}\text{Rb}$  via emitting  $\beta$  particle which de-excites to  $^{85}\text{Rb}$  emitting 0.514 MeV  $\gamma$  ray with 2.06  $\mu\text{s}$  mean lifetime. Its concentration is determined using  $^{85}\text{Kr}$  -  $^{85\text{m}}\text{Rb}$  coincidences resulting in an upper limit and from spectral fit described later in chapter 5. For the period used in the analysis, the upper limit is determined to be 9.8 cpd/100ton at 95% CL.

#### $^{238}\text{U}$ chain

$^{238}\text{U}$  is the prevalent radioactive isotope of uranium with natural abundance of 99.3%. It has mean life of 6.45 billion years. Its decay chain contains 8  $\alpha$  and 6  $\beta$  decays and ends with the creation of stable nuclei of  $^{206}\text{Pb}$ . Assuming the secular equilibrium, its concentration is measured by means of fast  $^{214}\text{Bi}$ - $^{214}\text{Po}$  coincidence tag:



$^{214}\text{Bi}$  and  $^{214}\text{Po}$  are produced in  $^{238}\text{U}$  decay chain itself via decay of  $^{222}\text{Rn}$ . After purification, the contaminant levels has significantly reduced to level:  $^{238}\text{U} < 9.4 \times 10^{-20}$  g/g (95% CL) [19]. Hence, its contribution can be said to be negligible for the analysis.

## <sup>232</sup>Th chain

<sup>232</sup>Th is the primordial isotope of natural Thorium with abundance of 100%. It has mean lifetime of 20.3 billion years. Its concentration in detector is determined by usage of <sup>220</sup>Rn (product in <sup>232</sup>Th decay chain) daughters decay sequence i.e <sup>212</sup>Bi-<sup>212</sup>Po coincidence tag:



After purification, the contaminant levels has significantly reduced to level: <sup>232</sup>Th < 5.7 × 10<sup>-19</sup> g/g (95% CL) [19]. This represents the concentration of about 10 orders of magnitude smaller than in any material on Earth.

## <sup>210</sup>Pb/<sup>210</sup>Bi

<sup>210</sup>Bi is the daughter nuclei of <sup>210</sup>Pb (eq 33). <sup>210</sup>Pb, which is not in equilibrium with <sup>238</sup>U decay chain, is present in detector since it can be absorbed by plastic and metal surfaces. <sup>210</sup>Bi has short mean lifetime of 7.23 days and decays to <sup>210</sup>Po via emitting  $\beta$  particle with end-point at 1.16 MeV. It is an important background to be considered in CNO analysis since its spectral shape is similar to the electron recoil spectrum of CNO- $\nu$ s which will be extensively discussed later in chapter 4. Due to this reason, the upper limit from an independent analysis on <sup>210</sup>Bi is determined. However, it is to be noted that the purification campaign has reduced its contamination by a factor of 2.3.

## <sup>210</sup>Po

<sup>210</sup>Po is a mono-energetic 5.3 MeV  $\alpha$ -emitter with mean lifetime of 200 days. However, due to strong quenching effects of the scintillator, its spectrum spans in the low energy region of <sup>7</sup>Be, CNO, *pep* and *pp* neutrinos. The spectral shape of <sup>210</sup>Po is a Gaussian peak and its spatial distribution is found to be non-uniform throughout the detector. There has been 2 sources of <sup>210</sup>Po in the detector. One is through the direct decay of <sup>210</sup>Pb/<sup>210</sup>Bi which will be referred to as supported Po. While the other component which is not in equilibrium with <sup>210</sup>Bi decay. This has been thought to be residual <sup>210</sup>Po brought by washing off surfaces of pipes and tanks used in purification campaign period and this is referred to as unsupported Po. It is also found that <sup>210</sup>Po is getting detached from the inner vessel surface and is referred to as convective Po. Since it is the only  $\alpha$  decay background, this characteristic has been used to determine its rate via pulse shape discrimination technique, being used widely in this thesis. Hence, it helped in deducing the upper limit on <sup>210</sup>Bi.

## External Backgrounds

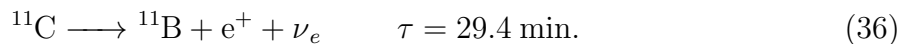
Background events that are generated outside the scintillator are referred to as external backgrounds. The sources of these external backgrounds is the radioactivity of the material surrounding the scintillator, for example, vessel support structure, PMTs etc. The  $\gamma$  decay of <sup>208</sup>Tl, <sup>214</sup>Bi and <sup>40</sup>K represent as the external background for CNO-analysis. In order to reduce their contribution for the analysis, a region of fiducial volume (FV) (Fig 3.4) is defined. Their exponential radial dependence is exploited in the fit method described in chapter 5 to deduce their contribution in the data.

## Cosmogenic Backgrounds

$^{11}\text{C}$  is one of the crucial background for CNO- $\nu$  analysis. It is produced by interaction of cosmic muons on  $^{12}\text{C}$  via emission of free neutron as :



and  $^{11}\text{C}$  further decays via positron emission:



The electron recoil spectrum of this background in the detector ranges from 1.02 MeV and 1.98 MeV which lies in the region of interest for CNO- $\nu$ s. The neutron produced in eq. 35 is captured with mean lifetime of 254  $\mu\text{s}$  on hydrogen emitting 2.2 MeV  $\gamma$  rays. Due to the deep underground location of Gran Sasso laboratory, only few tens of  $^{11}\text{C}$  nuclei are expected to be produced per day in the fiducial volume. Other cuts are applied to suppress its content in data as discussed later in section 4.1. Further reduction of its contribution is done by another algorithm called as Three Fold Coincidence (TFC) method which tag  $^{11}\text{C}$  through spatial and time coincidence with muons and captured neutrons as explained in chapter 4. The remaining  $^{11}\text{C}$  component is removed by pulse shape discrimination methods.

There are also other isotopes which are produced cosmogenically in the detector such as  $^{10}\text{C}$ ,  $^8\text{He}$ ,  $^9\text{Li}$  etc.

## 2.4 Data Acquisition

As seen in section 2.1, there are two data acquisition systems: Inner Detector (ID) composing of 2212 PMTs, facing radially inwards to collect the scintillation light inside Stainless Steel Sphere and Outer detector (OD) that consists of 208 PMTs detecting Cherenkov light produced by muons in water. They are further integrated using complex electronics and trigger systems.

Inner Detector (ID) electronics is organised in 14 identical racks, each of them handling 160 PMTs. Each rack contains the high voltage system to power the PMTs, front-end electronics connected to each PMT producing the signals and are further processed by the digital boards with backplane board that acts as an interface to the trigger system, often termed as Laben boards. The number of photoelectrons collected by Borexino detector is  $\sim 500$  p.e./MeV. Taking into account the energy range used for analysis, Borexino PMTs work mostly in single photoelectron regime. The signal due to single photoelectron at the front-end input is a pulse having an amplitude of about 12-15 mV and a total width of 15 ns.

The information related to energy deposition during a scintillating event is in total charge collected at the PMTs. The front end electronics integrates the signal via integrator whose signal is AC coupled with PMT signal and is fed into FADC system. The digital electronics provides the amplitude and time to digital conversion for each front-end channel. Here, the data is saved temporarily in internal buffer and the system waits for trigger. When trigger is fired, Borexino Trigger Board (BTB) delivers a trigger signal. The trigger should fire when at least 20 PMTs are hit within 100 ns trigger time window. Further, trigger record is written in VME readable memory with labelling of each event with unique 16

bits event number. For Outer Dectector, the front end electronic boards generate signal whose height is proportional to number of channels fired in coincidence. The Muon Trigger Board sends signal to BTB when at least 6 PMTs are fired in a time window of 150 ns [17].

After the data is stored, offline data processing is carried out by ROOT and C++ based software called as "Echidna" [20]. Its main tasks are decodification of the raw information, clustering of events, energy and position reconstruction of the event, and computation of particle identification tags used for pulse shape discrimination.

## Clustering

As we have seen, an event in Borexino is collection of hits on PMTs occurring within a time window with a long tail. However, during this time window, the random noise hits of 2212 PMTs also get recorded. Hence, a software procedure called clustering was developed to identify the scintillation pulse's beginning and its end. A cluster is a collection of hits belonging to same scintillation event. This clustering procedure allows to measure the time difference between close events with precision of less than 1 ns by identifying the time position of rising edge of each cluster. Event is selected only if single cluster is identified by the algorithm. This means that two uncorrelated events lying in same trigger window, referred to as "pile-up events" are also selected. In addition to that, clustering selects the fast coincidences like  $^{214}\text{Bi}$ - $^{214}\text{Po}$  coincidence tag (section 2.3).

## Energy and Position Reconstruction

The information about the energy of the event is in number of detected photoelectrons as PMTs of Borexino mainly works in single photoelectron regime. There are several energy estimators being used for the analysis:  $N_p$  - Total number of hit PMTs in the event,  $N_h$  - Number of detected hits including multiple hits on same PMT, and  $N_{pe}$  - Total charge collected by each PMT anode, that is, the number of photoelectrons (p.e). As the number of working channels vary as function of time, the energy estimators used in the analysis and simulation procedures are normalised to 2000 PMTs as :

$$N_{p,h,pe}^{norm} = \frac{2000}{N_{livepmts}} \times N_{p,h,pe}^m, \quad (37)$$

where  $N_{livepmts}$  is the number of working PMTs and  $N_{p,h,pe}^m$  is the measured value of the energy estimator. It is to be noted that for 1 MeV event,  $N_{p,h,pe}^{norm} \approx 500$ .

There is another energy estimator used for the analysis in this thesis known as geometrically normalised energy variable ( $N_{p,h,pe}^{geonorm}$ ). This is an another way to normalise the energy estimators. Here, the energy variable is normalised to a value proportional to the solid angle corresponding to the dead PMT with respect to the reconstructed event position. This normalisation has been found useful for the analysis of  $^{210}\text{Po}$  due to its non-uniform spatial distribution in detector. It was seen that this normalised energy estimator makes the peak of  $^{210}\text{Po}$  energy spectrum stable over time.

An energy response function is defined to establish a relation between the estimator and reconstructed variable. This was done using the calibration methods using radioactive materials [24]. There are several other factors too affecting the light production in scintillator like quenching effects and geometrical shadowing effects and hence affecting energy reconstruction.

The position reconstruction of the event is done by measuring the arrival times of photons on each PMT. An algorithm for this purpose is used that determines vertex position  $\vec{r}_0$  of the interaction using the arrival times of photons on each PMT and the position vectors  $\vec{r}_j$  of these PMTs. From each measured time  $t_i^j$ , a position dependent time of flight  $T_{flight}^i$  from interaction point to PMT  $j$  is subtracted. Then, maximisation of the likelihood that event occurs at position  $\vec{r}_0$  and time  $t_0$  given the measured hit space-time pattern  $(\vec{r}_j, t_i^j)$  is done using probability density functions (pdfs) of the hit detection.

### Pulse Shape Discrimination

The time distribution of photons emitted by scintillator depends on energy losses by a particle type. This feature is exploited to distinguish between different particle types such as  $\alpha/\beta$  and  $e^+/e^-$  by defining different shape variables. This method is effectively used to remove background component from the signal.

The discrimination method for  $\alpha$  and  $\beta$  particles makes use of the fact that in scintillator mixture used by Borexino,  $\alpha$  pulses are slower and have longer tail with respect to  $\beta/\gamma$  pulses. A neural network algorithm based on Multi Layer Perceptron (MLP) is applied to distinguish between the scintillation pulses of  $\alpha$  and  $\beta$  pulses with high efficiency. Fig 2.3 shows the distribution of MLP variable for  $\alpha$  and  $\beta$  events. The value of MLP parameter lies between 0 ( $\alpha$ ) and 1 ( $\beta$ ).

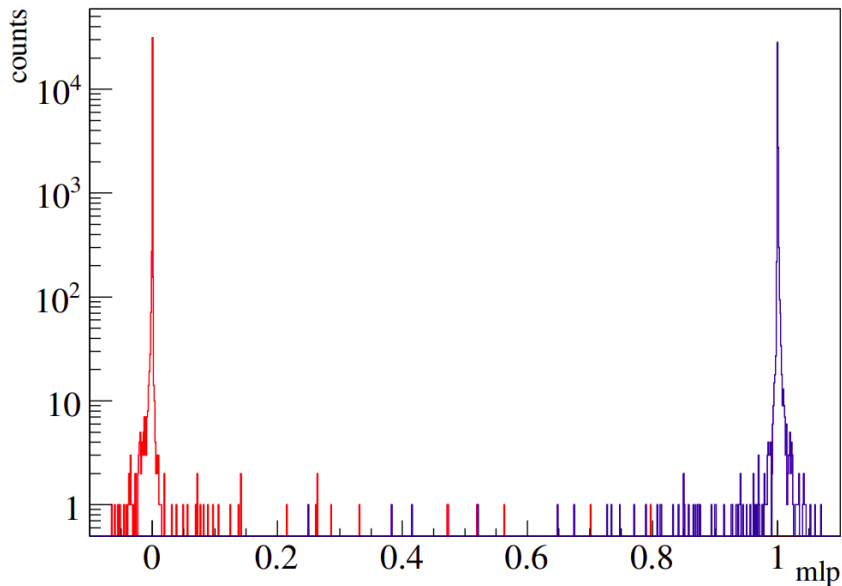


**Figure 2.3:** Distribution of MLP parameter for  $\alpha$  and  $\beta$  events from  $^{214}\text{Bi}$ - $^{214}\text{Po}$  coincidence [21].

Electron and positron events can also be distinguished on the basis of the time distribution of their scintillation pulses. There are reasons behind this difference: 1) In about half of the cases, positron produces ortho-positronium which results in delay of its annihilation by 3 ns. 2) The positron energy deposition occurs in multiple sites within the detector due to annihilation producing  $\gamma$  rays. These effects delay and extend the time distribution of scintillation photons for positrons with respect to electron events as shown in Fig 2.4. This discrimination is done using parameter called  $\text{PS-}\mathcal{L}_{\mathcal{PR}}$  defined as maximum value of likelihood function used in position reconstruction divided by value of

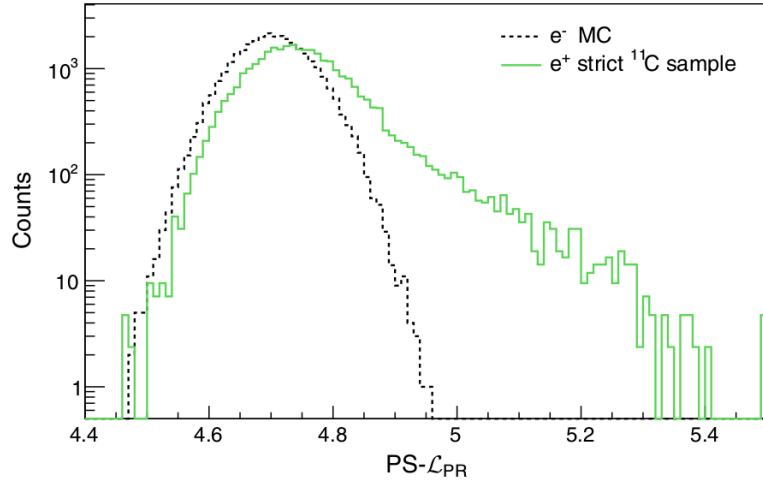


**Figure 2.4:** Distribution of  $\text{PS-}\mathcal{L}_{\mathcal{PR}}$  parameter for electron (obtained from simulation) and positron events (selected from strict  $^{11}\text{C}$  data) [19].

$N_p$  to remove energy dependence. It makes use of the scintillation light emission PDFs of electrons.

## Chapter 3

# Monte Carlo Simulation of the Detector

This chapter describes in detail the Monte Carlo software used for the simulation of the Borexino detector and my work related to the corrections needed for the simulation of  $^{210}\text{Po}$  events.

Section 3.1 introduces the program used for the simulation. The tasks performed by this simulation code and its structure are illustrated in this section. In section 3.2, the process of tuning and validation of MC input parameters are described. I performed the validation for the combined Phase 2 and Phase 3 data which is described in this section.

Section 3.3 explains the procedure used to produce the probability distribution functions (PDFs) which are used in the fitting method described in chapter 5. The method of normalisation particularly used for  $^{210}\text{Po}$  PDFs is detailed in section 3.4. This section also discusses my work on the tests performed to find the reason behind the triggering inefficiencies of simulated  $^{210}\text{Po}$  events.

### 3.1 Introduction to simulation code

The Monte Carlo (MC) simulation package of Borexino detector [23], based on GEANT4, simulates the geometrical design of Borexino and all the physical processes occurring inside the detector such as energy loss of particles inside detector components, production and propagation of scintillation photons inside the scintillator, their detection by photomultiplier tubes and the response of the readout electronics.

The Monte Carlo simulation chain of code is a set of numerical codes that perform the following tasks:

- Event generation such as solar neutrino interactions, radioactive decays, geo-neutrinos and calibration source events.
- Simulation of loss of energy of each particle in all detector materials (scintillator, buffer liquid, water in muon detector and in passive components).
- Generation of scintillation or Cherenkov photons taking into account the amount of energy loss in the media and the properties of scintillator and buffer.
- Tracking of each optical photon produced until it reaches the PMT or is absorbed after the interaction with materials.
- Generation of PMT response for photon absorption at PMT cathode, considering the quantum efficiency of each PMT.

- Generation of PMT pulse signal, considering the front-end and digital electronics design of Borexino.
- Simulation of trigger generation and saving of final output for triggering events.
- Production of raw data file with same structure as the one produced by the Borexino data acquisition system (section 2.4).

The MC code is technically structured into the following separate programs:

### **Event Generation and Light Tracking**

The feature of event generation is implemented within Geant4 package called as "g4bx2". This package also allows to define the geometry and construction materials of Borexino detector in the simulation. Its libraries allows to simulate radioactive decay chains and energy losses of all types of particles and to generate the event by producing the optical photons. However, the decays of  $^{210}\text{Bi}$  and  $^{14}\text{C}$  are treated differently from that of Geant4 standard approach. For this purpose, event generators are developed to simulate their beta decay spectrum with a shape factor which accounts for differences in various decay models. The interaction of these photons like absorption, reemission, scattering and their tracking until their detection by PMTs is also taken into account by the simulation.

### **Simulation of Readout Electronics**

The electronics simulation code, known as "bxelec", produces the simulation of electronics chain of Borexino and its trigger system response, based on the information of the PMT pulse times and considering its quantum efficiency (QE). This simulation code takes into account the loss of PMTs and acquisition boards in order to follow the real time evolution of electronics of Borexino detector. This code also takes into account the changing QE of PMTs due to their aging and also the change in the light yield of scintillator by calculating EQE i.e "effective quantum efficiency" [31] on a periodic basis. The same trigger evaluation conditions as of the detector is simulated by this code. The simulated data is saved in the format of real data. However, the number of simulated events exceeds the number of events in real data to neglect the effect of statistical uncertainty.

### **Reconstruction of Simulated data**

Finally, the simulated data goes through processing by the same code "Echidna" (section 2.4) which also analyses the real data. The reconstruction of simulated data into physical observables is done using Echidna and are saved in the same format. Here, some true input parameters regarding the simulated event (known as "McTruth parameters") are also stored.

## **3.2 Tuning and Validation of MC code**

Monte Carlo simulation is crucial in solar neutrino measurements as it is used to produce the reference shapes that will be used in the fit method described in chapter 5. Hence, it is required that MC is able to reproduce the detector response as of the real detector. This requires the parameters defining the simulation to be properly tuned and validated on the basis of its performance. The MC was tuned and validated using calibration data.

The calibration campaign has taken place between years 2008 and 2011 [24]. This included internal and external calibration campaigns helped in studying the energy response of the detector. The sources used for the internal calibration are mono-energetic  $\gamma$  sources (whose energy ranges from 0.122 MeV to 1.46 MeV),  $^{222}\text{Rn}$ - $^{14}\text{C}$  source,  $^{241}\text{Am}$ - $^9\text{Be}$  source and laser sources. These sources were placed at different locations inside the detector to study the energy scale, validation of MC simulations and testing position reconstruction algorithm.  $^{228}\text{Th}$  source was exploited as the external calibration source which aided in the study of determination of inner vessel shape and distribution of  $\gamma$  emitting external backgrounds. In addition to this, the laboratory setups also contributed in studying detector's energy response.

## Tuning of MC

A part of the calibration data was used to optimise input parameters of MC simulation which describes various features of scintillator and its materials like attenuation lengths, refractive indexes etc. The three steps used for tuning the MC includes measurement of non-uniformity in energy response, study of time distribution of collected light and reproduction of the absolute energy scale. The remaining part of the calibration data is used to test the performance of the simulation.

## Validation of MC

The validation of MC simulation can be done either using a set of calibration data independent from the one used for tuning or using data from standard data taking. One of the method which is used for validation of MC makes use of  $\alpha$  decays of  $^{210}\text{Po}$ . The  $^{210}\text{Po}$  events lying in fiducial volume (Fig 3.4) were selected from data using MLP parameter (section 2.4) and a sample of  $^{210}\text{Po}$  events were simulated using MC using the same spatial distribution as of data. Further, the Gaussian energy distributions of  $^{210}\text{Po}$  in geonormalised energy estimator (chapter 4) in data and MC are compared and this led to the determination of spectral position of the peak which aided in studying energy scale stability over time. From Fig 3.1, it can be concluded that the input parameters of MC simulation are properly tuned to reproduce the real data, and the scintillator response for MC agrees with that of real data within precision level of 1% except for the year 2019. This implies that if difference between energy scale of MC and data continues to disagree at a level of more than 1% level, the MC input parameters are needed to be re-tuned from this year onwards. The precision level of disagreement in the  $^{210}\text{Po}$  peak in data and MC, is taken into account as systematic error which is explained in chapter 6.

## 3.3 Construction of MC PDFs

In order to disentangle solar neutrino signal and backgrounds from the data, the reference spectrum of each component is required. These reference spectra are the probability density functions (PDFs) which are produced using Monte Carlo simulation. The following steps (Fig 3.2) are taken to construct these PDFs:

- After event generation and reconstruction by Echidna (section 3.1), the simulated data for signal and background species are saved as ROOT files for each run<sup>1</sup>.

---

<sup>1</sup>Each run corresponds to typically 6 hours of data taking.

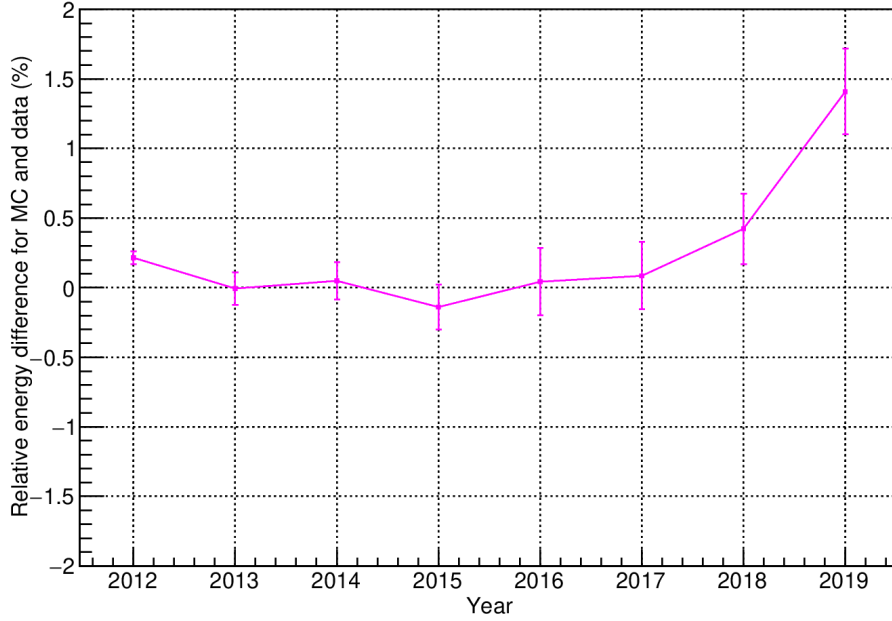


**Figure 3.1:** Figure shows the time evolution of relative difference (%) in energy position of  $^{210}\text{Po}$  peak. The spectral position of the  $^{210}\text{Po}$  peak in data and MC is found to be in agreement ( $\sim 1\%$ ) until year 2018.

- The next step is to apply the event selection cuts like muon cut, fiducial volume cut etc discussed in the next chapter. These cuts (referred to as "nusol cuts") are exactly same as of the real data selection used for the solar analysis.
- For each species, the output for each run is summed together to have a single output for a particular period.
- In the last step, the resulting summed histogram is normalised to take into account all the detector effects. Hence, MC PDFs are constructed.

### Normalisation of PDFs

Normalisation of PDFs is crucial for species whose spectrum lies in the low energy region. It is so because in low energy region, triggering and clustering effects come into play and hence, changing the spectral shape of the species in case of a real detector. This is well depicted in Fig 3.3. To get correct rate of interaction of the solar neutrinos or background component, normalisation is necessary. Normalisation is done using normalisation factor ( $f_N$ ) which is defined as the ratio of the number of reconstructed and triggered events ( $N_{reco}$ ) lying in fiducial volume (FV) that passes the nusol cuts to the number of events generated in FV (Fig 3.4) ( $N_{genFV}$ ):

$$f_N = \frac{N_{reco}}{N_{genFV}}. \quad (38)$$

### 3.4 Normalisation of $^{210}\text{Po}$ PDFs and Study of triggering inefficiency

The events of all solar neutrino and background species like  $^{210}\text{Bi}$ ,  $^{85}\text{Kr}$ ,  $^{11}\text{C}$  etc are generated uniformly in the detector. So, their PDFs are normalised according to equation

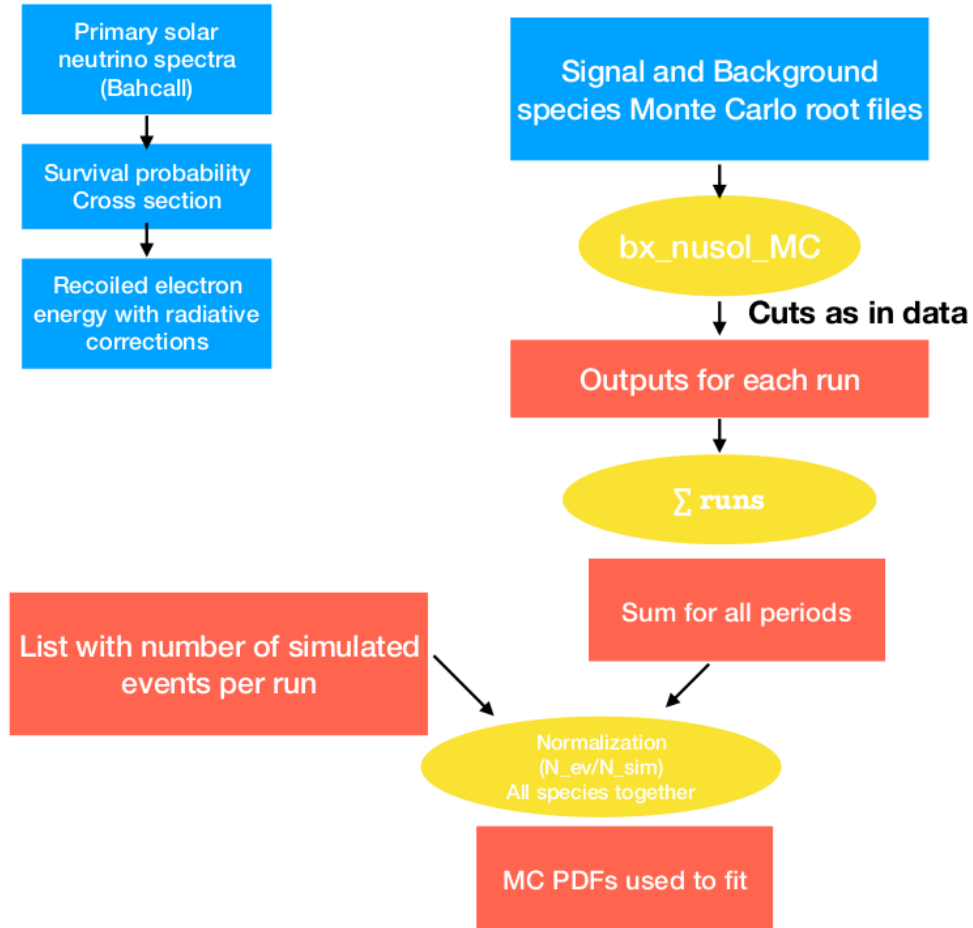


**Figure 3.2:** Figure shows the procedure to construct PDFs from MC simulated data [28].

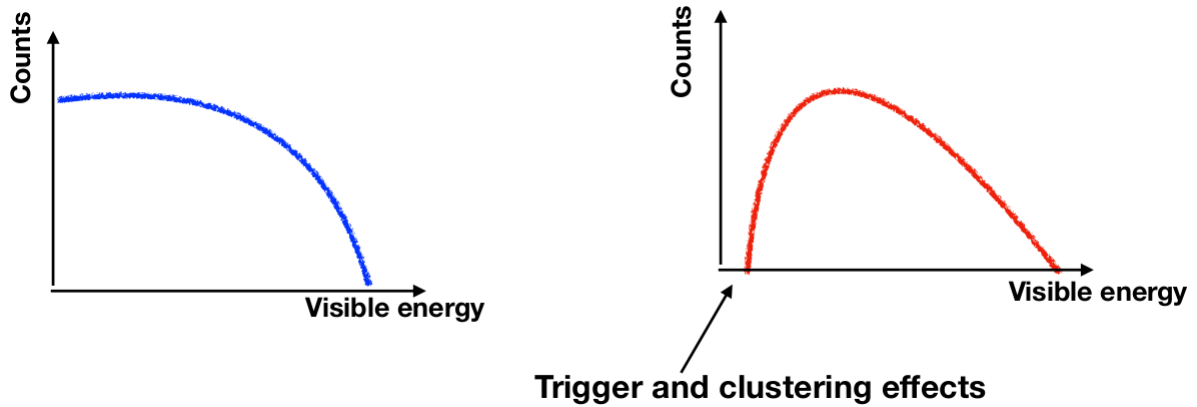


**Figure 3.3:** The figure shows the spectrum on left (Blue) shows the PDF before normalisation while the spectrum on right (Red) shows the PDF after normalisation.

38 where  $N_{genFV}$  is calculated as:

$$N_{genFV} = N_{genTOT} \frac{V_{FV}}{V_{gen}}, \quad (39)$$

where  $N_{genTOT}$  is the total number of events that were generated in MC simulation,  $V_{FV}$  and  $V_{gen}$  represent the fiducial volume (FV) and generation volume (mostly Inner Vessel (IV)) respectively.

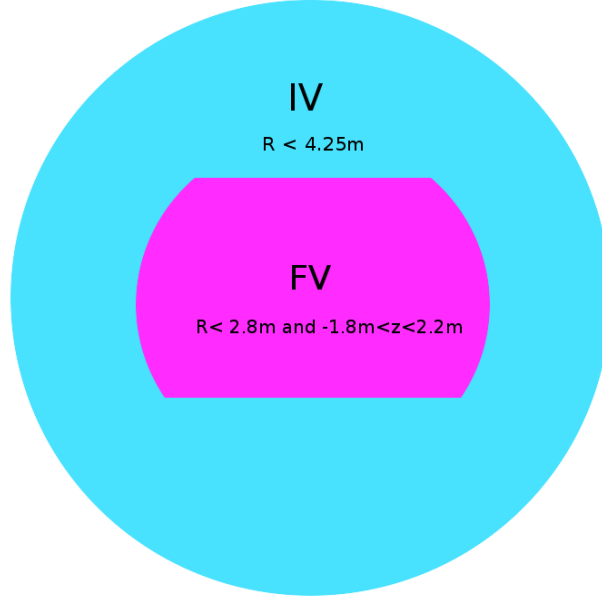


**Figure 3.4:** The figure shows the shape of the fiducial volume (FV) inside Inner vessel (IV).

However, the scenario is different for  $^{210}\text{Po}$ . In reality,  $^{210}\text{Po}$  events are distributed non-homogeneously throughout the detector. This means that number of events cannot be assumed to be proportional to the volume in which they are generated. Hence, the spatial distribution of simulated data is based on the spatial distribution of reconstructed data (referred to as "Pomap" and shown in Fig 3.5). The Pomap is produced by applying both energy cut of  $150 \leq N_p^{norm} \leq 230$  and a mlp cut on data. So,  $^{210}\text{Po}$  PDFs are normalised according to equation 38 where  $N_{genFV}$  is calculated as:

$$N_{genFV} = N_{genTOT} \frac{N_{FV}}{N_{IV}}, \quad (40)$$

where  $N_{genTOT}$  is the total number of events that were generated in MC simulation,  $N_{FV}$  and  $N_{IV}$  represents the number of events from data lying in the fiducial volume (FV) and Inner Vessel (IV) respectively.

It is to be noted that the principle of using equations 39 and 40 (and not the "Mc-Truth parameters") to calculate the number of events generated in FV is to take into account also the events which were generated in FV but did not trigger at least a PMT. For the sake of statistics, a Gaussian smearing is applied on each event in Pomap to produce "PoSmearMap" (Fig 3.6). Hence, the number of events lying in FV and IV are selected to evaluate the ratio of  $N_{FV}$  and  $N_{IV}$  in equation 40.

The calculated values of normalisation factor ( $f_N$ ) in equation 38 for each period is tabulated in Table 3.1 (as  $f_N$  before optimisation). Here, one can see the decreasing trend of normalisation factor from  $\sim 98\%$  to  $\sim 88\%$  which one doesn't expect in reality. It is so because energy spectrum of  $^{210}\text{Po}$  lies well above the trigger threshold ( $N_h^{norm} > 20$ ). Therefore, normalisation factor is expected to be  $\sim 100\%$  (at a precision level of 1-2%) for all the periods of time.

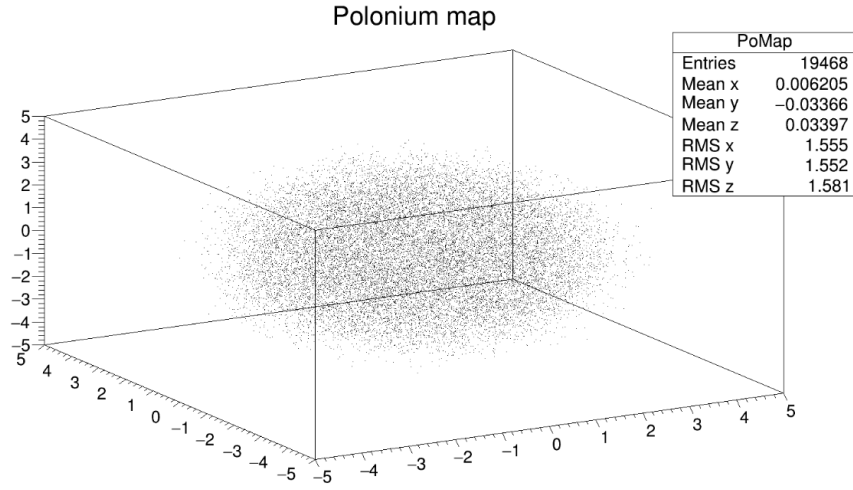


**Figure 3.5:** The spatial distribution of Po in real data in Dec 2011.

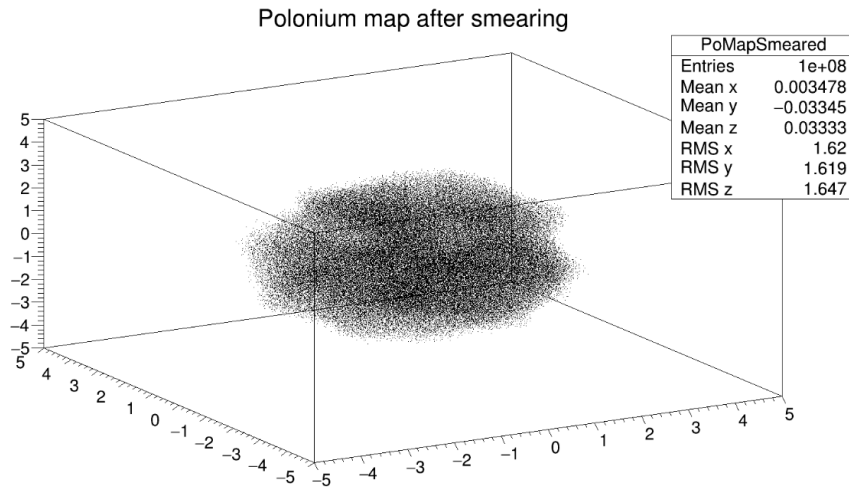


**Figure 3.6:** The spatial distribution of Po after Gaussian Smearing of events in Fig 3.5.

Looking into this issue has led to the conclusion that the problem is related to changing Inner Vessel shape with respect to time. There was a leak of scintillating medium from the inner vessel to buffer region detected in 2008 by measuring high content of PPO in buffer region [18]. This leak caused density and pressure difference between scintillator and buffer and hence, resulted in the deformation of IV shape. The original shape of IV is shown in Fig 3.4 and the deformed shapes in 2012 and 2019 is shown in Fig 3.7.

It was observed that in the MC simulation for  $^{210}\text{Po}$ , some of the events were generated outside the inner vessel as shown in Fig 3.8 and Fig 3.9 and these events resulted in no trigger (Fig 3.10). The deformation of IV shape has been evolving over time (Fig 3.7). The MC simulation by default takes into account the change in IV shape. However, this was not followed by MC for the case of  $^{210}\text{Po}$  due to the incorrect usage of 3D maps. This caused an increase in the percentage of events to lie in the buffer region with respect to time and hence, resulted in lesser number of events to trigger above threshold. However, it was seen that this problem was not present for other species.

The MC code was optimised to solve this problem. The events generated after optimisation of MC code are shown in Fig 3.11 and Fig 3.12. The normalisation factors for  $^{210}\text{Po}$

Period	$f_N$ before optimisation	$f_N$ after optimisation
2012	0.9805	0.9990
2013	0.9705	1.0250
2014	0.9610	1.00
2015	0.9492	0.9891
2016	0.9153	0.9957
2017	0.8922	0.9941
2018	0.8819	1.0136
2019	0.8825	1.0242

**Table 3.1:** Value of Normalisation factors (eq 38) for  $^{210}\text{Po}$ .

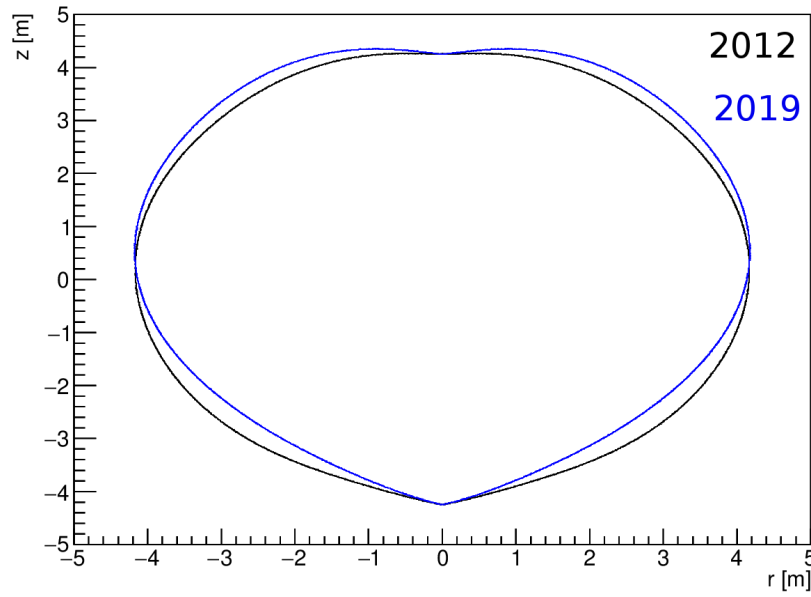


**Figure 3.7:** Figure shows the IV shape in 2012 (Black) and in 2019 (Blue) with z-direction on vertical axis and  $r = \sqrt{x^2 + y^2}$  on horizontal axis of the plot where x,y and z corresponds to detector axis.

PDFs were calculated again and are tabulated in Table 3.1 (as  $f_N$  after optimisation). The normalisation factor for some years is greater than 100% due to reconstruction of the events inside the fiducial volume that would have lied outside of it.

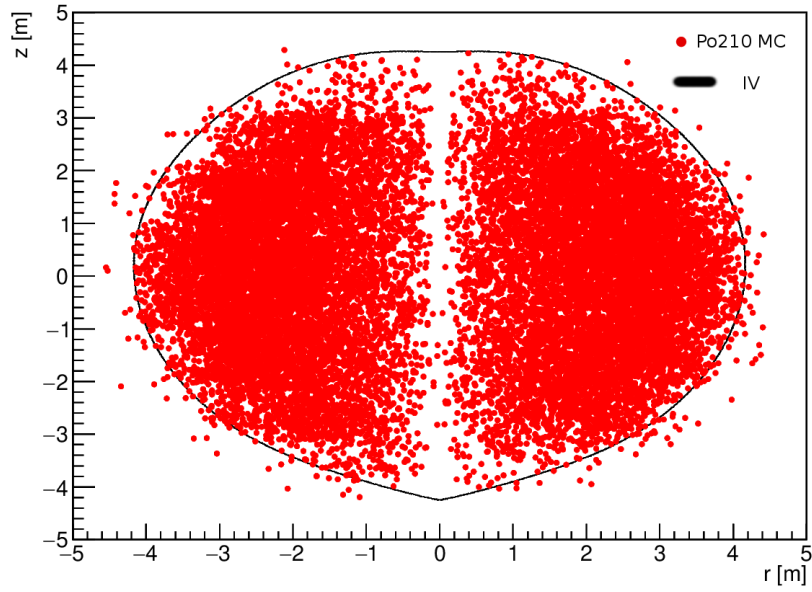


**Figure 3.8:** The figure shows the z-r distribution of MC generated  $^{210}\text{Po}$  events in year 2012 compared to IV shape.

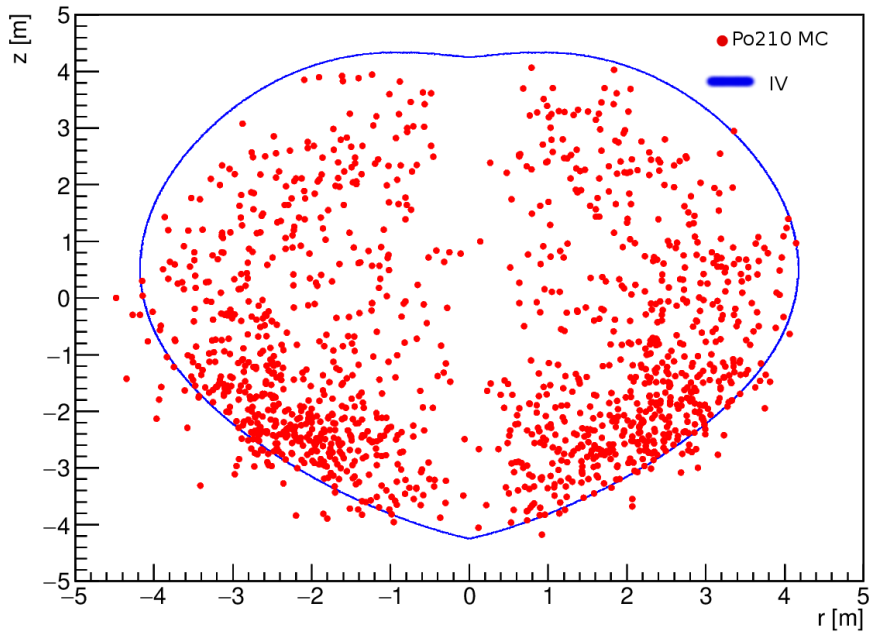


**Figure 3.9:** The figure shows the z-r distribution of MC generated  $^{210}\text{Po}$  events in year 2019 compared to IV shape.

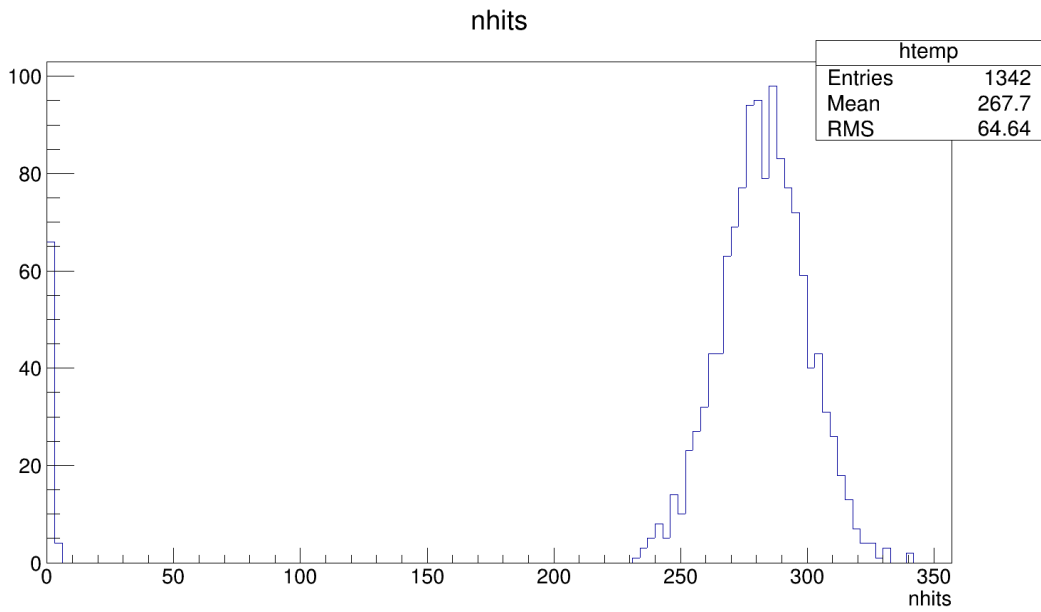


**Figure 3.10:** The figure shows the nhits distribution of MC generated  $^{210}\text{Po}$  events (before `bx_elec`). One can see the events lying below trigger threshold of 20 nhits.

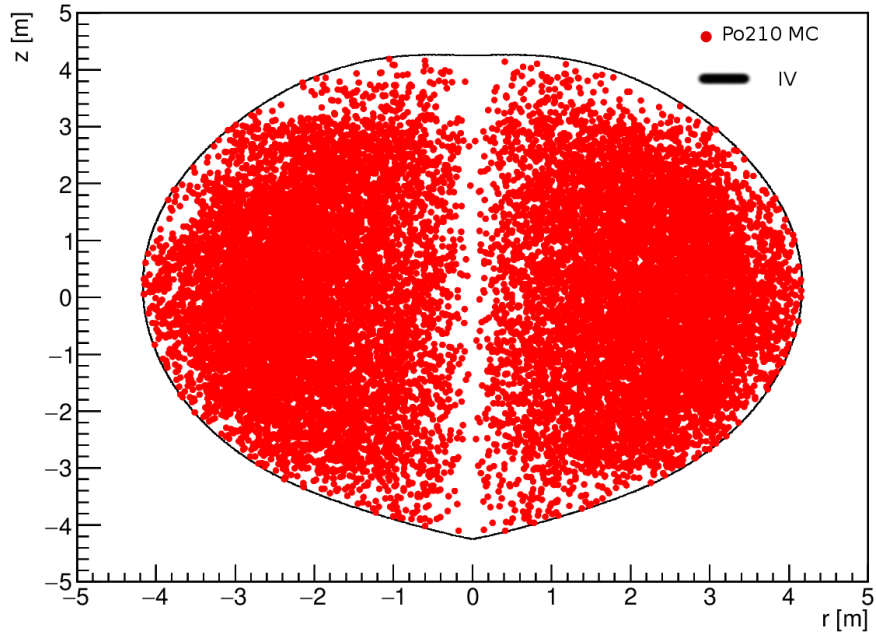


**Figure 3.11:** The figure shows the z-r distribution of MC generated  $^{210}\text{Po}$  events in year 2012 compared to IV shape after optimisation of simulation code. One can see that no events lie outside the IV.

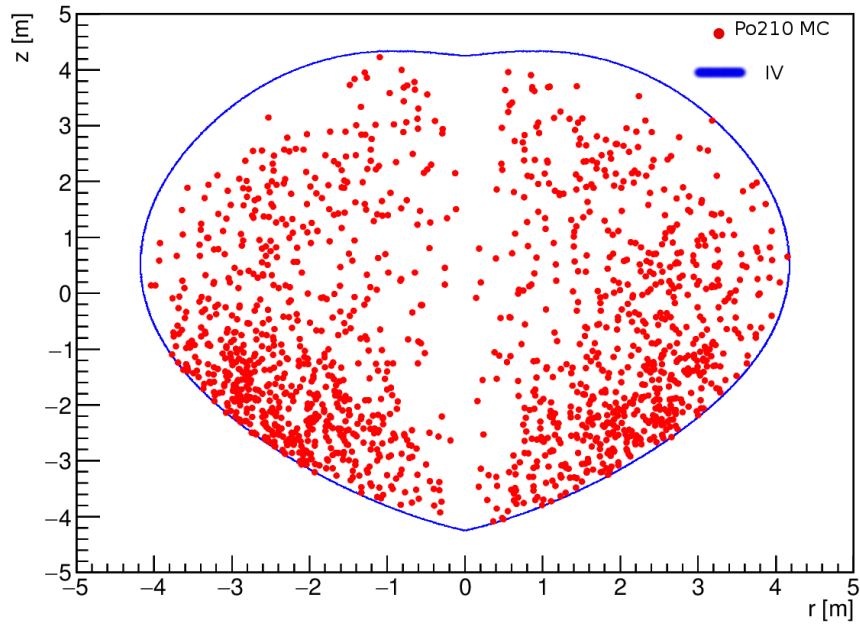


**Figure 3.12:** The figure shows the z-r distribution of MC generated  $^{210}\text{Po}$  events in year 2019 compared to IV shape after optimisation of simulation code. One can see that no events lie outside the IV.

## Chapter 4

# Analysis Strategy: Data Selection and Constraints

This chapter introduces the strategy used for CNO- $\nu$  analysis which composed of selection cuts applied to combined signal and background data, and the conditions on rate of interaction of some species which will be used in the fit.

The dataset used for CNO- $\nu$  analysis and the selection cuts applied to this dataset for reducing background contribution are described in sec 4.1. In subsection 4.1.1, an important technique of tagging cosmogenic  $^{11}\text{C}$ , called as Three Fold Coincidence, is described with its usage in the analysis. This subsection also illustrates my work on determining  $^{11}\text{C}$  shift value i.e the value in nhits by which PDF of  $^{11}\text{C}$  needs to be shifted in order to match the peak of  $^{11}\text{C}$  energy spectrum in PDF to that of in data.

In section 4.2, the constraints on background rates required for the analysis and the methods used to determine their values are discussed. The important constraints for the CNO- $\nu$  analysis are the value of interaction rate of  $pep-\nu$ , and an upper limit on  $^{210}\text{Bi}$  rate. The interaction rate of  $pep-\nu$  is determined on the basis of SSM as discussed in section 4.2.1. The technique implemented to evaluate an upper limit on  $^{210}\text{Bi}$  rate is illustrated in section 4.2.2. Here, I will describe my work on determination of parameters related to model used to evaluate this constraint and their importance. These parameters include the efficiency of MLP parameter used for pulse shape discrimination of  $\alpha/\beta$  events.

### 4.1 Data Selection

The CNO- $\nu$  analysis is based on the Phase 3 data (chapter 2) which spans from June 2016 till February 2020. The total exposure of this data set is 1072 days  $\times$  71.3 tonnes. This data undergoes several cuts in order to remove various backgrounds and non-physical events. The data selection cuts used for CNO analysis are listed as following:

- **Muon and muon-daughter cut** - Muon events in the data are removed by this cut. As discussed in section 2.1, the deep underground location of Gran Sasso laboratory strongly suppresses the flux of muons arriving at the detector. However, additional cuts are applied for further reduction in its contribution in data. This is done using information from muon veto in Outer detector (OD) and Inner detector (ID). Since muon passing ID often saturates the electronics, whole detector is vetoed for 300 ms after each muon is identified. Muons passing the OD are removed and a 2 ms veto of the whole detector is applied. This helps in the reduction of cosmogenic neutrons

and other spallation products.

- **Single cluster cut** - As described in section 2.4, a physical neutrino event in the detector corresponds to single cluster event. Events with zero cluster or more than one cluster correspond to non-physical events and are rejected by the clustering algorithm.
- **Fiducial volume cut** - Fiducial Volume (FV) is a software-defined region inside the inner vessel (Fig 3.4) which is exploited to maximise signal over background ratio. The main goal as pointed in section 2.3 is to suppress external background events. The region of FV used for CNO analysis is defined as  $r < 2.8$  m and  $-1.8$  m  $< z < 2.2$  m, where  $r$  is the radius and  $z$  corresponds to the vertical axis inside IV. The vertical cut is asymmetric in order to suppress the background from end-cap supports from top and bottom of IV taking into account the non-spherical shape of IV. This region contains 71.3 tonnes of scintillator mass. Hence, events lying only inside this region are selected for the analysis.
- **Coincident event cut** - In this cut, the events which are reconstructed within 1.5 m and occurring in 2 ms time window are removed. An additional energy cut is applied to remove Radon daughters ( $^{214}\text{Bi}$  -  $^{214}\text{Po}$  (section 2.3)). The energy cut of (180-3600) keV for  $^{214}\text{Bi}$  and (400-1000) keV for  $^{214}\text{Po}$  is applied [18].
- **MLP cut** - The noise events present in the data are removed by applying a MLP parameter cut ( $\text{MLP} > 0.1$ ) above  $^{210}\text{Po}$  energy region.
- **Qrec cut** - This cut removes the noise events by checking the mismatch between reconstructed charge and number of fired PMTs.

#### 4.1.1 Three Fold Coincidence (TFC) cut

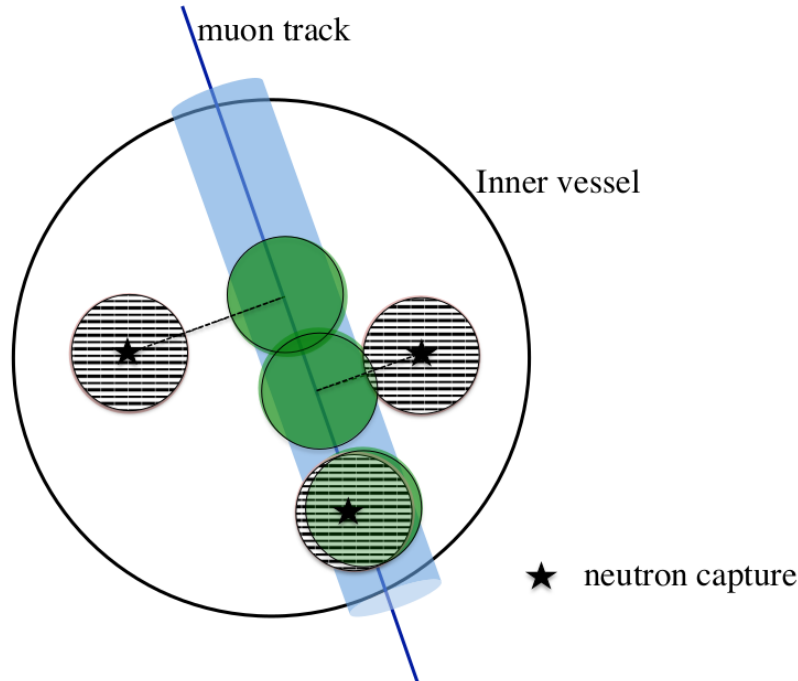


**Figure 4.1:** Figure shows the regions which are vetoed in TFC method [18]

As discussed in section 2.3,  $^{11}\text{C}$  is one of the major backgrounds for CNO analysis.  $^{11}\text{C}$  is produced by the interaction of cosmic muons with  $^{12}\text{C}$  in the detector and it decays via emission of positron. The neutron produced along with  $^{11}\text{C}$  (eq. 35) is captured by the hydrogen with lifetime of  $(254.5 \pm 1.8) \mu\text{s}$  [18] and emits 2.2 MeV  $\gamma$  rays. There is a residual amount of  $^{11}\text{C}$  events left in the data even after applying muon cut. These events are further reduced by the Three Fold Coincidence (TFC) technique. This method exploits the time and space correlation between muons, neutrons, and the subsequent  $^{11}\text{C}$  decays. The principle of this technique is as follows:

- A cylindrical veto of radius 80 cm is applied along the parent muon track for time window of 2 hours if neutron clusters or at least a neutron is found in muon gate.
- In case, a neutron is detected and has reliable reconstructed position, a spherical region of radius of 1 m centered at neutron position is vetoed for 2 hours. In addition to this, 1 m spherical veto is applied around the point on muon track which is closest from neutron capture position.

This is shown in Fig 4.1. This method gives a bool of 1 (if tagged event is  $^{11}\text{C}$  candidate) or 0 (if tagged event is not  $^{11}\text{C}$  candidate). This technique is referred to as TFC-MI (MI stands for Milano). There is an improved TFC technique, referred to as TFC-MZ (MZ stands for Mainz), which is based on the algorithm that evaluates the likelihood ( $\mathcal{L}_{\text{TFC}}$ ) that an event is a  $^{11}\text{C}$  candidate. This algorithm takes into account the observables like distance in space and time from parent muon, distance from neutron, neutron multiplicity, and muon dE/dx. Fig 4.3 shows the distribution of  $\mathcal{L}_{\text{TFC}}$  vs  $N_p^{dt1}$  (where dt1 corresponds to time interval of 400 ns).

## Usage of TFC

### Fitting of data

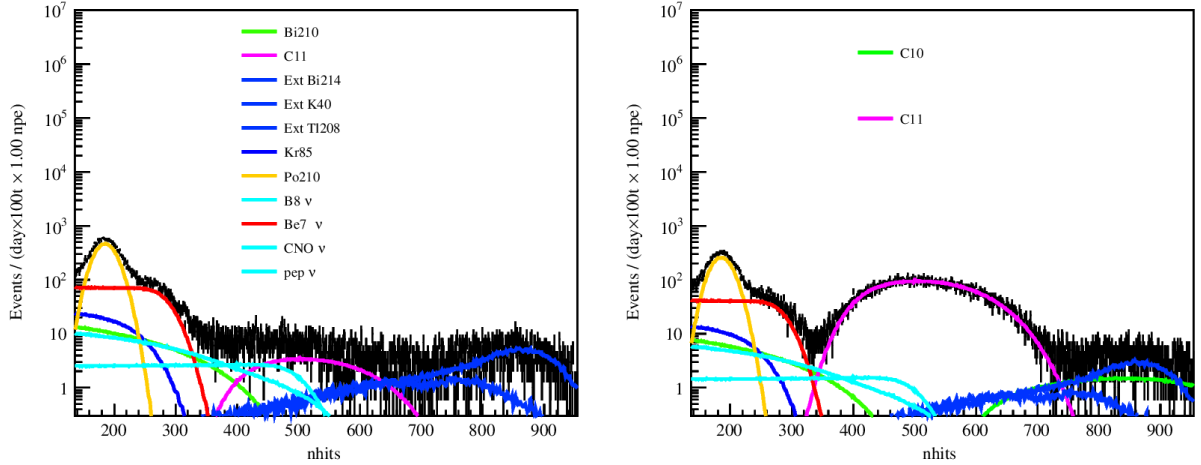


**Figure 4.2:** The figure shows the 2 sets of spectra- TFC-subtracted (on the left) and TFC-tagged (on the right). One can see the difference of the 2 spectra lies in the  $^{11}\text{C}$  region (shown in pink).

Using the TFC method, the data is divided into 2 sets of spectrum (Fig 4.2):

- *TFC-tagged spectrum* - this sample is enriched in  $^{11}\text{C}$  events containing  $\sim 36\%$  exposure.

- *TFC-subtracted spectrum* - this sample is depleted in  $^{11}\text{C}$  tagged events containing  $\sim 64\%$  exposure.

These 2 spectra are fitted using the multivariate fit method as explained in the next chapter. For TFC-MZ, the events which lie above the  $\mathcal{L}_{\text{TFC}}$  threshold (Fig 4.3) belongs to TFC-tagged spectrum while the events lying below  $\mathcal{L}_{\text{TFC}}$  threshold are assigned in TFC-subtracted spectrum.

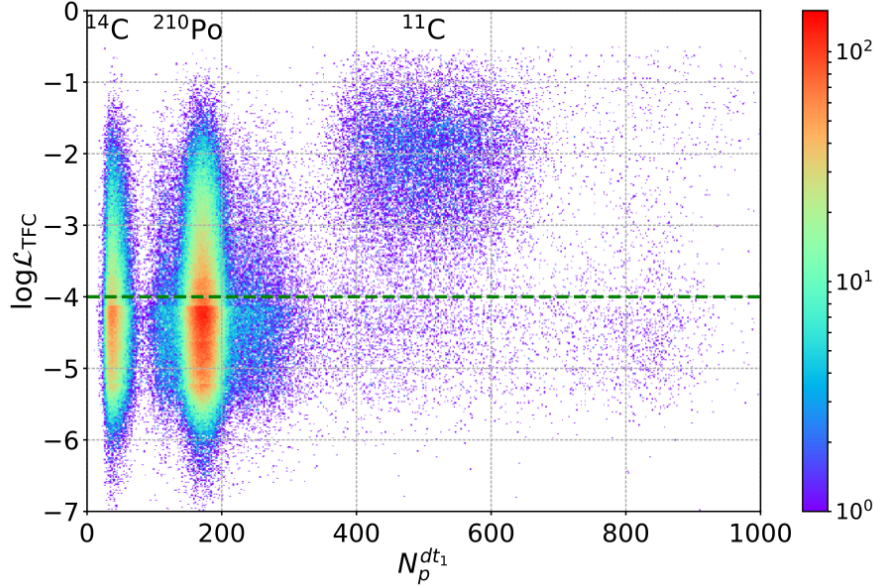


**Figure 4.3:** Figure shows the distribution of  $\mathcal{L}_{\text{TFC}}$  vs  $N_p^{dt1}$ . The green dashed line marks the  $\mathcal{L}_{\text{TFC}}$  threshold [19].

### $^{11}\text{C}$ shift

The other usage of TFC technique is to determine the value by which PDF of  $^{11}\text{C}$  shift has to be shifted. This is done because studies have shown that the peak of  $^{11}\text{C}$  in MC PDFs does not agree well with that of in data, which will be shown later.

The following method has been exploited to study  $^{11}\text{C}$  shift and determine its correct value. This is necessary to get overall good fit of whole data set which will be shown in next chapter. The steps in the method are as follows:

- The first step is to select  $^{11}\text{C}$  events from data using strict cuts such that the probability of tagging events from species other than  $^{11}\text{C}$  is very low. These strict  $^{11}\text{C}$  events are selected using Three Fold Coincidence (TFC) method. The Nhits ( $N_h$ ) distribution of  $^{11}\text{C}$  events is shown in Fig 4.4.
- Now, the Monte Carlo PDFs are prepared for  $^{11}\text{C}$  and other species which lie in the spectral region of  $^{11}\text{C}$  which are  $^7\text{Be}-\nu$ ,  $pep-\nu$ ,  $\text{CNO}-\nu$ ,  $^{210}\text{Bi}$  and external backgrounds (Fig 4.5).
- The MC distributions of all the species except  $^{11}\text{C}$ , and external backgrounds are added together and weighted according to HZ SSM predictions [19] or their independent estimations using analytical fit method described in [31]. This is shown in Fig 4.5. The values of their rate of interaction, which are used in the addition of

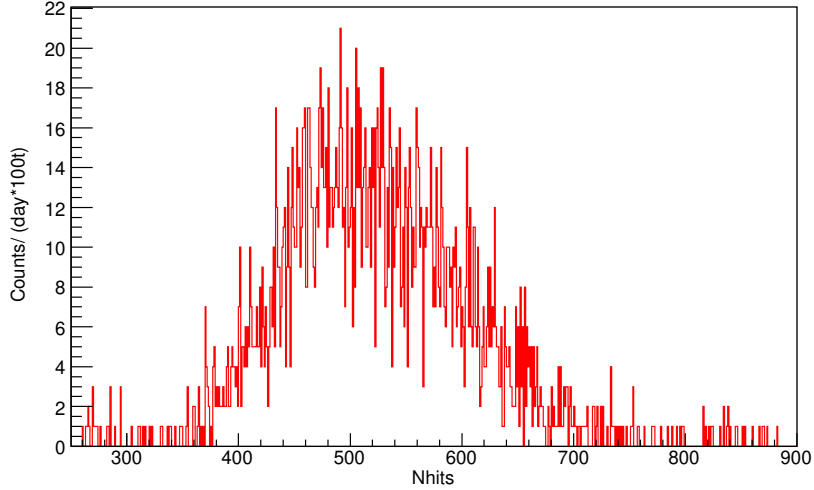


**Figure 4.4:** Distribution of strict  $^{11}\text{C}$  events in nhits selected from the data by TFC technique.

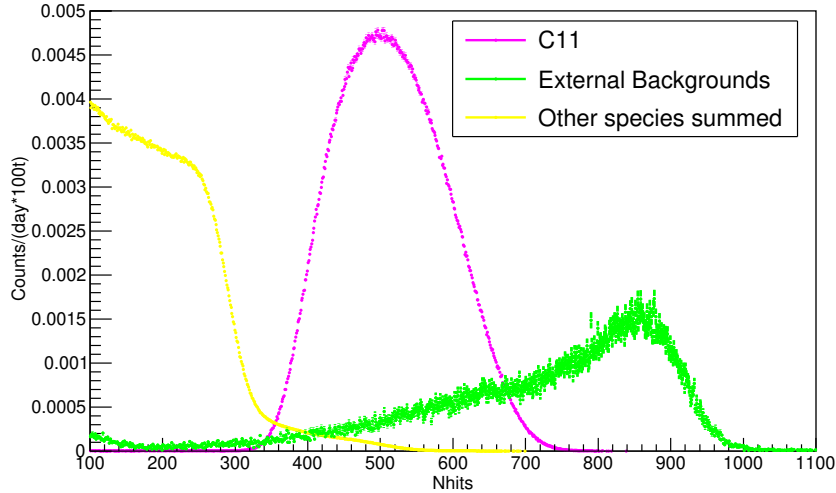


**Figure 4.5:** The figure shows MC reference shapes (PDFs) in normalized Nhits produced for  $^{11}\text{C}$  shift studies. The PDF for  $^{11}\text{C}$  is shown in pink while PDFs in green and yellow represent summed reference shapes for external backgrounds and other species like  $^7\text{Be}-\nu$ ,  $pep-\nu$ ,  $\text{CNO}-\nu$ , and  $^{210}\text{Bi}$  respectively.

their PDFs, are tabulated in Table 4.1. The distribution of  $^{11}\text{C}$  events represents the spectrum of positron events while the remaining represents the distribution of electron events. This feature of  $^{11}\text{C}$  events makes its PDF to be shifted.

- Further, the energy distribution of strict  $^{11}\text{C}$  data is fitted with all these PDFs in the energy range of 260-850 nhits. The fitting is done for several values by which PDF of  $^{11}\text{C}$  is shifted. Here, due to presence of some technicalities associated to binning of PDFs, non-integer values of shifts is achieved by shifting each event in PDF by that value. The best value is estimated from the likelihood profile as shown in Fig 4.6.
- One can see from Fig 4.6 that the optimised value of shift is  $5.0 \pm 0.7$  nhits. This amounts to a relative difference of  $(1 \pm 0.1) \%$  in peak position for  $^{11}\text{C}$  energy spectra

Species	Rate of interaction (cpd/100ton)
${}^7\text{Be}-\nu$	47.9
$pep-\nu$	2.74
CNO- $\nu$	4.92
${}^{210}\text{Bi}$	12.5
External ${}^{214}\text{Bi}$	4
External ${}^{208}\text{Tl}$	5
External ${}^{40}\text{K}$	0.5

**Table 4.1:** The value of rate of interaction for different species spanning in the energy region of  ${}^{11}\text{C}$ .

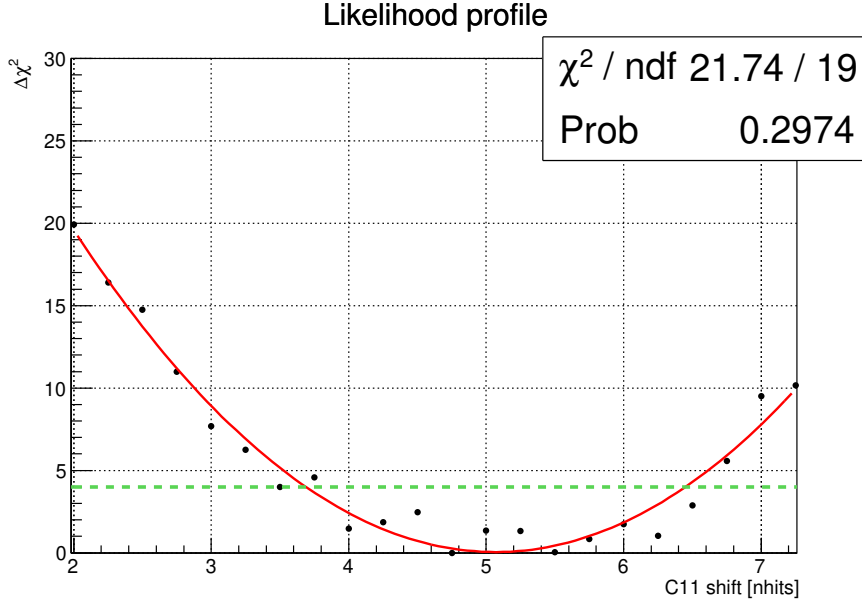


**Figure 4.6:** Figure shows the likelihood distribution for  ${}^{11}\text{C}$  shift values. The central value ( $\Delta\chi^2 = 0$ ) is 5.0 nhits with statistical uncertainty of 0.7 nhits at  $1\sigma$  significance level. This value is obtained by fitting set of points with parabola and the values shown on top right are goodness of fit parameters. The green dashed line corresponds to  $2\sigma$  significance used to estimate the error on  ${}^{11}\text{C}$  shift value.

in MC and data. The fit result corresponding to this shift value is shown in Fig 4.8. One can see the better distribution of residuals and better p-value (0.40) in Fig 4.8 compared to the Fig 4.7 where PDF of  ${}^{11}\text{C}$  is not shifted at all. This value is used in the fitting method described in the next chapter.

As the  ${}^{11}\text{C}$  shift value is fixed for the fitting of Phase-3 dataset, the studies regarding this shift value has been taken into account in the evaluation of systematics which is described later in chapter 6.

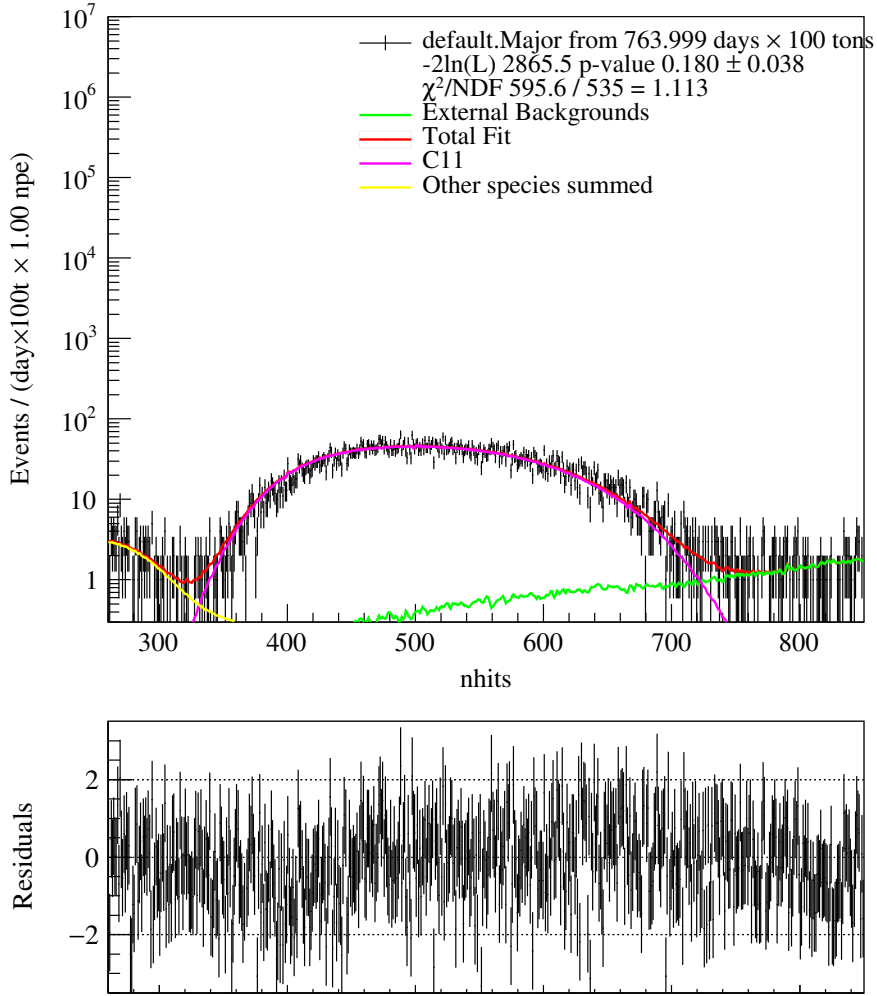


**Figure 4.7:** The figure shows the fit results of  $^{11}\text{C}$  strict data (at top) between the starting and ending region of  $^{11}\text{C}$  spectra without any shift of  $^{11}\text{C}$  PDF including the distribution of residuals at bottom. The PDFs are shown in colored legends.

## 4.2 Constraints

There are several parameters used in the analysis which are required to be constrained for the CNO- $\nu$  measurement. The important constraints for the CNO- $\nu$  analysis are the value of interaction rate of  $pep-\nu$ , and an upper limit on  $^{210}\text{Bi}$  rate which is described below. It is so because these interaction rates are found to be correlated with the rate of interaction of CNO- $\nu$ . This study was done using MC pseudo-experiments, and fitting those simulated data without any constraint using the method described in next chapter. One can see the strong correlation among their interaction rates [19] in Fig 4.10. This is because  $pep-\nu$ , CNO- $\nu$  and  $^{210}\text{Bi}$  have degenerate electron recoil spectrum in the detector as shown in Fig 4.9. Hence, the methods which are independent from the technique extracting CNO- $\nu$  signal have been exploited to determine these constraints as discussed in this section.

### 4.2.1 $pep-\nu$ constraint

The rate of interaction of  $pep-\nu$  is constrained on the basis of Standard Solar Model predictions for neutrino fluxes. Since the reactions producing  $pep-\nu$  and  $pp-\nu$  have same nuclear

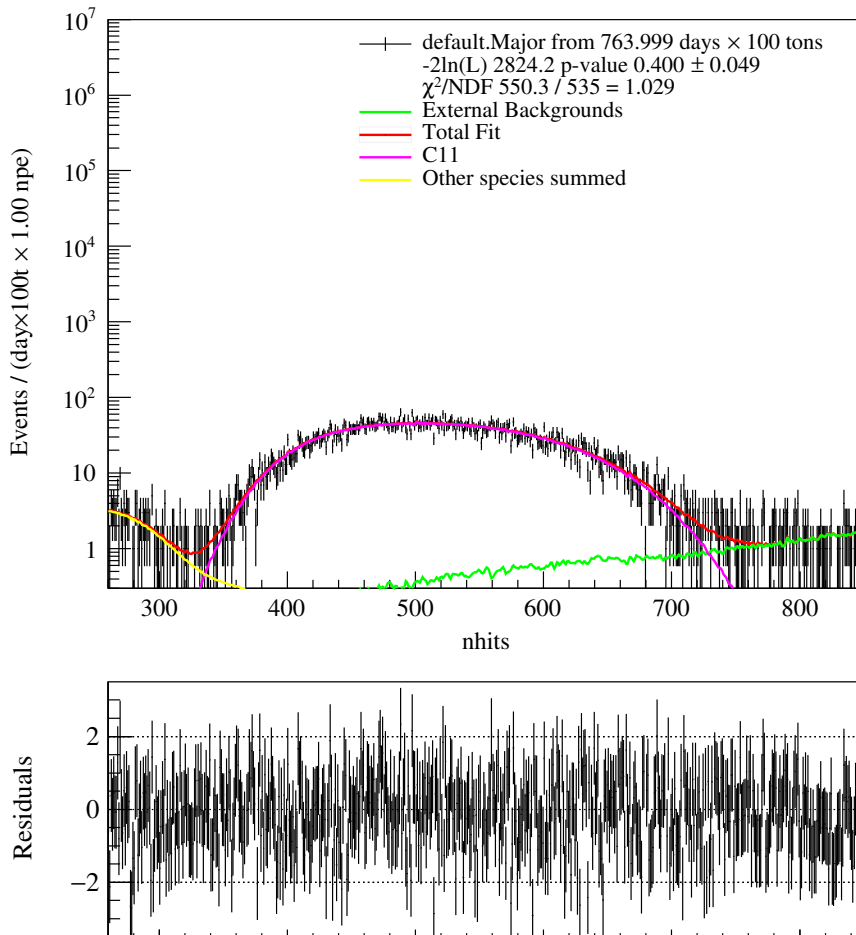


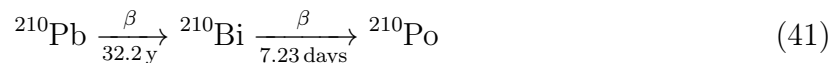
**Figure 4.8:** Figure shows the fit results when PDF of  $^{11}\text{C}$  is shifted by 5.0 nhits. One can see high p-value of 0.40 and better distribution of residuals than shown in Fig 4.3. The PDFs are shown in colored legends.

matrix element, the ratio of their fluxes and hence, the ratio of their interaction rates is known at 1% precision level. In addition to this, solar luminosity constraint ([25]-[26]) i.e the energy determined from solar luminosity is equal to the energy associated to solar neutrino flux, is used. Further, a global fit to data from all solar neutrino experiments is utilised to obtain the constraint on  $pep-\nu$  rate with a precision of 1.4%. Using this approach and considering the errors on oscillation parameters, the  $pep-\nu$  rate is constrained to the value  $(2.74 \pm 0.04)$  cpd/100t which is used for the CNO- $\nu$  analysis.

#### 4.2.2 Upper limit on $^{210}\text{Bi}$

As we see in Fig 4.9, the spectral shape of CNO- $\nu$  and  $^{210}\text{Bi}$  decay is almost similar. This poses a challenge in order to disentangle the CNO- $\nu$  contribution from the data. To constrain the  $^{210}\text{Bi}$  decay rate, the following approach has been adopted.

As described in the section 2.3,  $^{210}\text{Bi}$  is the daughter nuclei of  $^{210}\text{Pb}$  (section 2.3) with mean lifetime of 7.23 days and decay to  $^{210}\text{Po}$  as shown below:



$^{210}\text{Po}$  ends this chain by decaying into stable  $^{206}\text{Pb}$  via emitting  $\alpha$  particle as shown

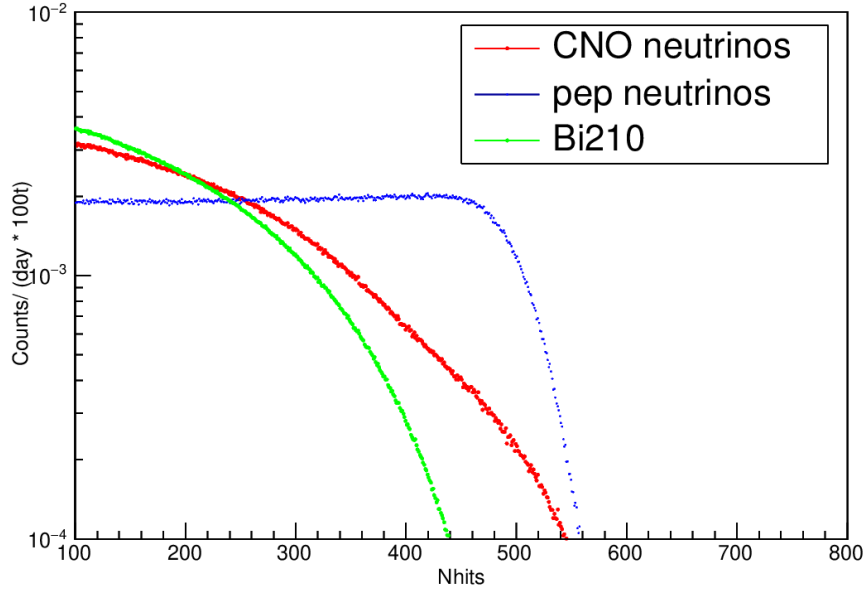


**Figure 4.9:** Figure shows the reference spectral shapes of  $pep-\nu$ ,  $CNO-\nu$  and  $^{210}\text{Bi}$  in normalized Nhits.

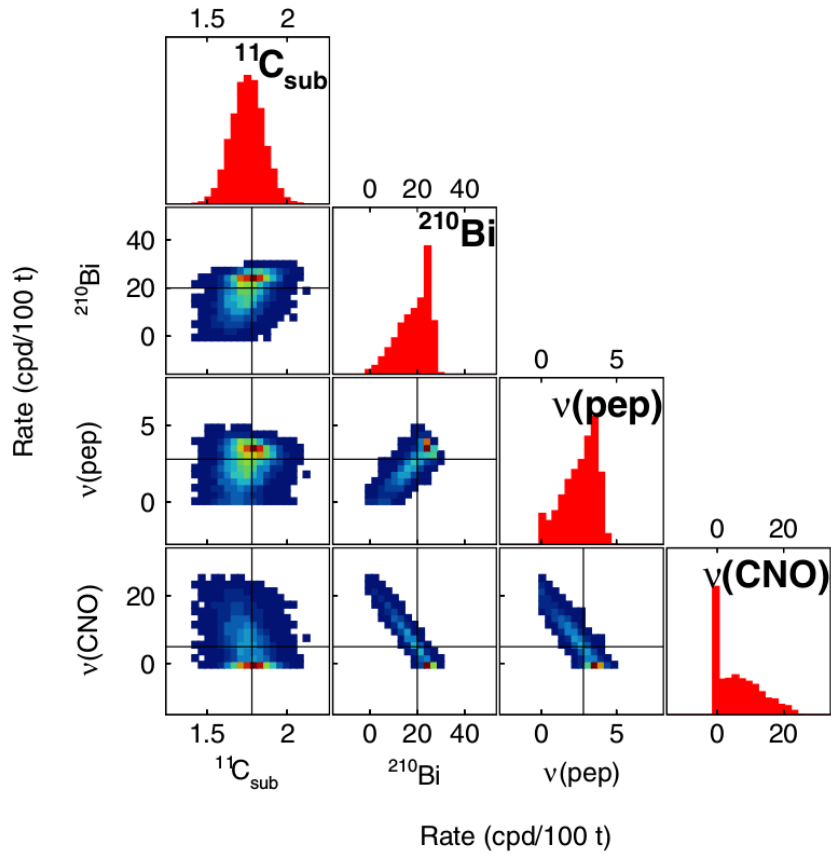


**Figure 4.10:** The figure shows the correlations between the rates of interaction of different species. One can see the strong correlation and anti-correlation among  $pep-\nu$ ,  $CNO-\nu$ , and  $^{210}\text{Bi}$  rate from non-diagonal plots [19].

below.



The  ${}^{210}\text{Po}$  events can be identified via  $\alpha$  particle using pulse shape discrimination technique as mentioned before. When these 2 equations are in secular equilibrium with each other,  ${}^{210}\text{Bi}$  rate is equal to the rate of  ${}^{210}\text{Po}$  decay. However, it was found out that there had been other sources of  ${}^{210}\text{Po}$  inside the detector in addition to  ${}^{210}\text{Pb}$  decay. The different sources of  ${}^{210}\text{Po}$  in the detector are listed as following:

- **Supported  ${}^{210}\text{Po}$ :** This component is in secular equilibrium with  ${}^{210}\text{Pb}/{}^{210}\text{Bi}$  present in detector.
- **Unsupported  ${}^{210}\text{Po}$ :** The Water Extraction phase during purification campaign has led to the contamination of the detector with  ${}^{210}\text{Po}$  since  ${}^{210}\text{Po}$  washed off the surfaces of pipes and storage tanks. Fortunately, this component has completely decayed away and hence, does not contribute for the analysis.
- **Convective  ${}^{210}\text{Po}$ :** The origin of  ${}^{210}\text{Po}$  in detector is also known to come from Inner Vessel surface.  ${}^{210}\text{Po}$  detaches from this surface and moves into FV either by diffusion or by convection. The effect of diffusion is found to be negligible. The component migrated to FV by convection is referred to as convective  ${}^{210}\text{Po}$  (Fig 4.11).

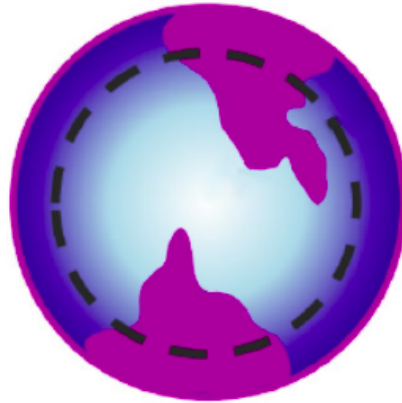


**Figure 4.11:** Figure shows the graphic representation of migration of  ${}^{210}\text{Po}$  from IV surface due to convection [27].

It was seen that the convective currents of  ${}^{210}\text{Po}$  resulted in the fluctuations of  ${}^{210}\text{Po}$  activity in FV. This leads to the difficulty in the determination of  ${}^{210}\text{Bi}$  rate. The reason for these convective currents has been associated to the seasonal variations in the temperature and human activities affecting temperature of Hall C where detector is installed in Gran Sasso laboratory. Hence, the temperature is needed to be controlled in order to make it stable for reducing the contamination of inner volume of scintillator by  ${}^{210}\text{Po}$ .

To achieve this goal, a vertical thermal gradient was established. The Borexino detector is installed above a heat sink provided by the rock with temperature of  $7.5^\circ\text{C}$  while its temperature of its top is  $15.8^\circ\text{C}$ . However, the instability in air temperature required a thermal insulation campaign to be conducted in the year 2015 in order to achieve this stable temperature gradient. Between May and December 2015, the Borexino Water Tank



Figure 4.12: The figure shows the detector after thermal insulation<sup>1</sup>.

was covered with 2 layers of mineral wool as shown in Fig 4.12.

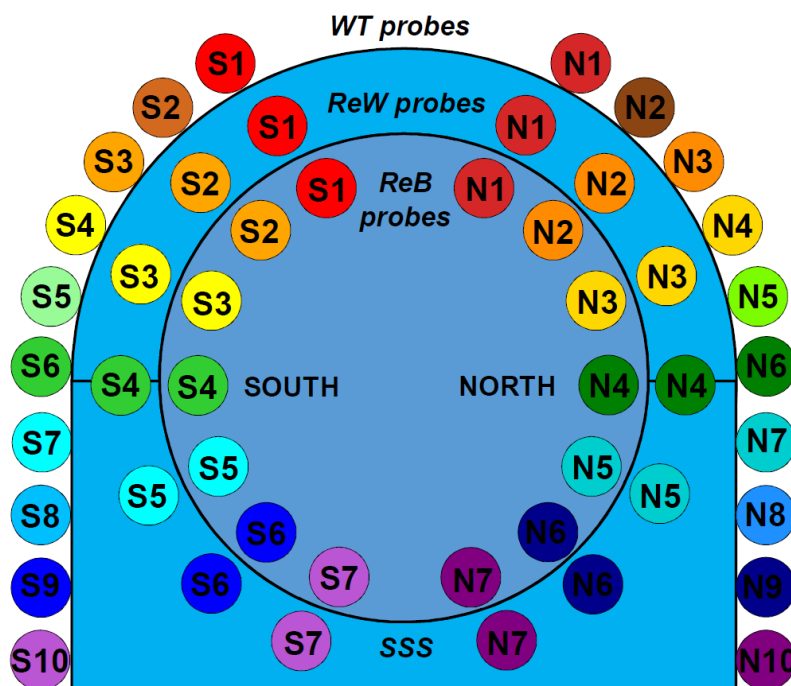


Figure 4.13: Figure shows the different locations of probes monitoring the temperature of the detector<sup>2</sup>.

An Active Temperature Control System has been installed on the top of water tank to provide for compensating the seasonal cooling in winters. In order to monitor the detector

<sup>1</sup>Source: Borexino Collaboration

<sup>2</sup>Source: Borexino Collaboration

temperature, the detector was equipped with temperature sensors at different positions as shown in Fig 4.13. This work concerning stabilizing the inner detector temperature has resulted in the stabilization of  $^{210}\text{Po}$  background for the CNO analysis. This is depicted in Fig 4.14. In this figure,  $^{210}\text{Po}$  rate is calculated using layers of iso-volume cylindrically symmetric to z-axis referred to as z-slices [28].

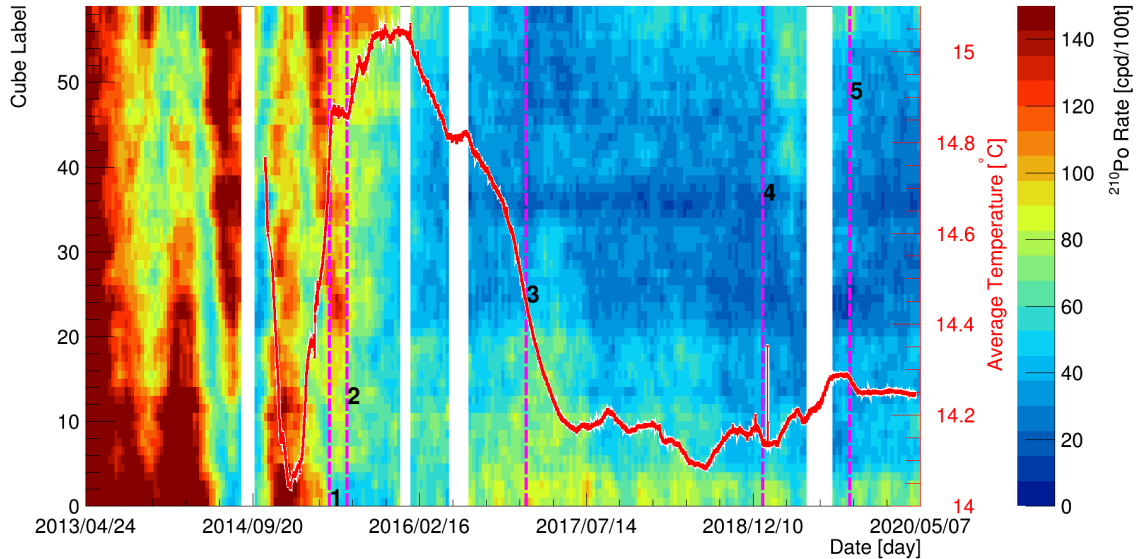


**Figure 4.14:** The figure shows the time distribution of  $^{210}\text{Po}$  rate in small cubes of about 3 tonnes ordered from 0 (bottom) to 58 (top of the detector). Fluctuations with high rate of  $^{210}\text{Po}$  are present until year 2015. The red curve with its red scale on the right represents the average temperature in the innermost region surrounding the nylon vessel. The dashed vertical lines indicate the most important milestones of the temperature stabilisation program: 1. Beginning of the “Insulation Campaign”; 2. Turning off of the water re-circulation system in the Water Tank; 3. First operation of the active temperature control system; 4. Change of the active control set point; 5. Installation and commissioning of the Hall C temperature control system. The white vertical bands show different DAQ interruptions due to technical issues.

From Fig 4.14, it can be seen that after thermal insulation, the seasonal convective currents have reduced which resulted in the creation of a region (blue) where  $^{210}\text{Po}$  rate is minimum. This region is referred to as Low Polonium Field (LPoF) with mass of 20 tons where contribution from residual convective motions is very low. Hence,  $^{210}\text{Po}$  rate in LPoF is sum of the contribution from supported  $^{210}\text{Po}$  ( $R(^{210}\text{Bi})$ ) and residual convective  $^{210}\text{Po}$  ( $R(^{210}\text{Po}^V)$ ) i.e

$$R(^{210}\text{Po}_{\min}) = R(^{210}\text{Bi}) + R(^{210}\text{Po}^V). \quad (43)$$

The minimum value of  $^{210}\text{Po}$  rate which is used to evaluate upper limit on  $^{210}\text{Bi}$  rate is calculated on the Phase 3 dataset. LPoF region resembles the ellipsoidal shape with symmetry along x-y plane. Due to residual convective current in LPoF which results in the small movement of LPoF along z-direction of the detector, the center of this ellipsoid also changes over time. To tackle this, the data of every month is fitted with following

paraboloidal function ([29]-[30]) and is aligned using the previous month:

$$f(\theta) = \frac{M \cdot t}{100} \cdot (R(^{210}\text{Po}_{\min}) \cdot \text{eff}_\alpha + \beta_{\text{leak}}) \cdot \left[1 + \frac{\rho^2}{a^2} + \frac{(z-z_0)^2}{b^2}\right], \quad (44)$$

where  $M$  represents mass of fit region,  $t$  is live-time of data in days,  $\beta_{\text{leak}}$  is the leakage of  $\beta$  events due to MLP selection,  $\text{eff}_\alpha$  is efficiency of MLP parameter for  $\alpha$  events selection,  $a$  and  $b$  are the paraboloidal axes,  $z_0$  is the position of minimum and  $\rho^2 = x^2 + y^2$ .

My work here concentrates on the determination of the parameters  $\text{eff}_\alpha$  and  $\beta_{\text{leak}}$ , which are fixed in the equation 44. These are the crucial parameters to be determined for the analysis because absence of these parameters could lead to the wrong determination of  $^{210}\text{Po}$  rate and in turn resulting in the negative bias of  $^{210}\text{Bi}$  rate. These are discussed below.

### MLP efficiency

The parameter  $\text{eff}_\alpha$  is referred to as MLP efficiency to correctly identify  $\alpha$  events. The following test shows that the condition on data using MLP parameter may remove some  $\alpha$  events and hence, discards  $^{210}\text{Po}$  events in data. In order to study and determine this efficiency parameter for the dataset used in the fit of  $^{210}\text{Po}$  data, the same cut of energy and MLP is applied on MC generated  $^{210}\text{Po}$  events as of applied in the method used to fit  $^{210}\text{Po}$  data. The cuts include  $150 < N_{pe}^{\text{geonorm}} < 270$  and  $\text{MLP} < 0.3$ . This test have shown that 96.9% of the pure  $^{210}\text{Po}$  events were identified as  $\alpha$  events and hence, the efficiency of MLP parameter to tag  $\alpha$  events is 96.9% which is used in equation 44.

### Beta leakage

The studies on calibration data [32] has shown that the MLP parameter cut of  $\text{MLP} < 0.3$  misidentifies some of the  $\beta$  events as  $\alpha$  events and hence, can lead to leakage of other species in  $^{210}\text{Po}$  data during selection. In order to take this into account, the parameter  $\beta_{\text{leak}}$  is used in equation 44.

There are 2 methods which have been adopted to determine this parameter. Those are listed as follows:

- **Gaussian and Exponential fit** - This method uses simple Gaussian model to fit  $^{210}\text{Po}$  data and an exponential function to determine contribution of  $\beta$  events in  $^{210}\text{Po}$  data. The exponential function is used because the studies based on calibration sources regarding MLP parameter cut of less than 0.3 have shown that tagging of  $\beta$  events as  $\alpha$  events by MLP has exponential dependency with respect to energy ([32]-[33]). For this technique, same cuts of MLP and FV described above are applied to  $^{210}\text{Po}$  data. The fit result for best possible configuration is shown in Fig 4.15. From this fit, the rate of  $\beta$  events in energy region ( $150 < N_{pe}^{\text{geonorm}} < 270$ ) chosen for analysis for minimum  $^{210}\text{Po}$  rate is 2.05 cpd/100 ton. The systematic error associated to this method is evaluated by varying the energy range of fit and hence, the final result is  $2.1 \pm 0.4$  cpd/100 ton.
- **Fit using MC PDF** - There is a drawback in using the simple Gaussian and exponential function as model to fit data that it assumes flat  $\beta$  spectrum in the energy region of  $^{210}\text{Po}$  due to dominance of  $^7\text{Be}-\nu$  spectrum. However, this was not found to be the case as depicted in Fig 4.17. So, an independent technique is

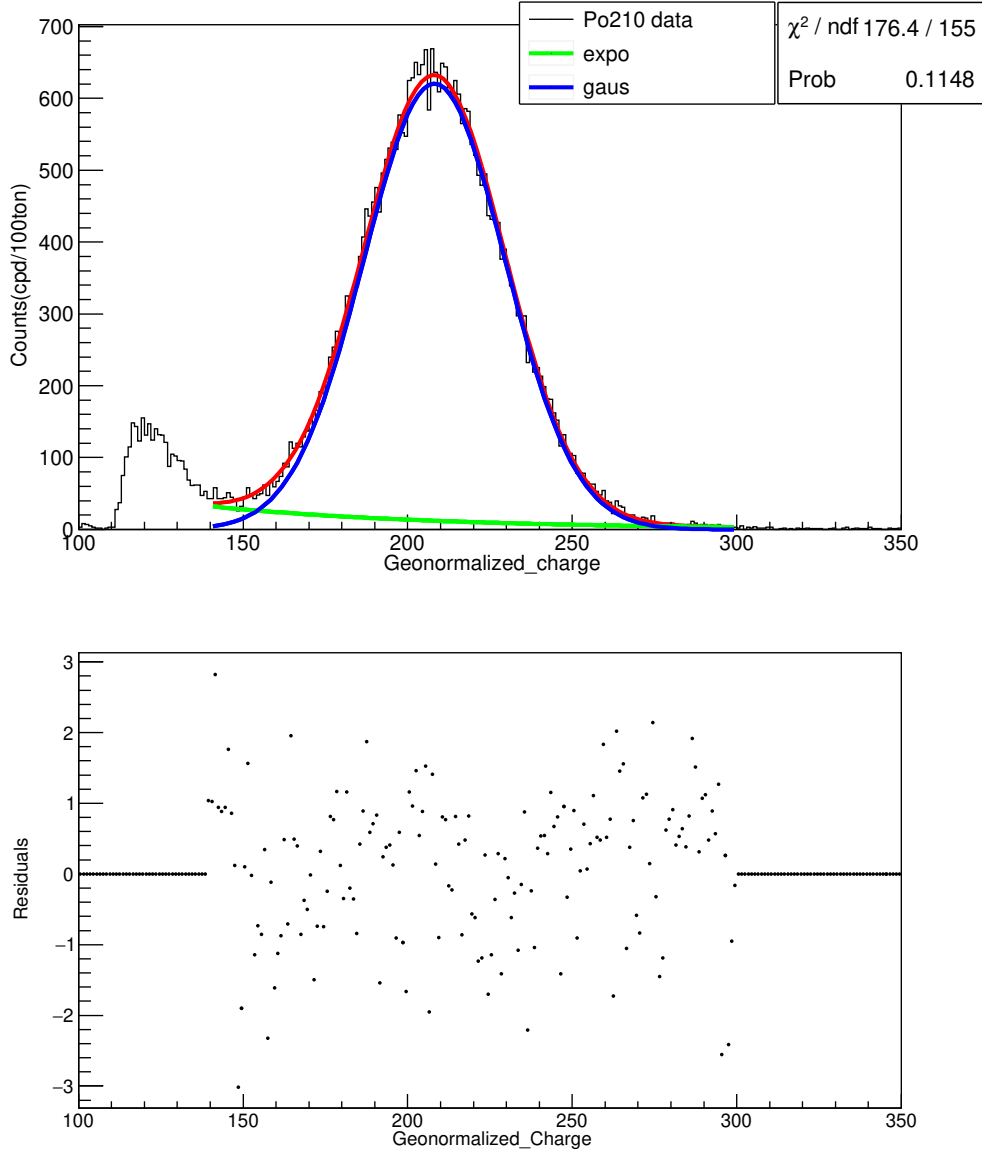


**Figure 4.15:** The figure shows the best fit result on  $^{210}\text{Po}$  data for the estimation of  $\beta_{leak}$  using simple Gaussian and exponential model including the residuals at bottom.

developed to crosscheck the above method and used, which does not rely on such assumption. The details of this method are as follows.

- First, the  $^{210}\text{Po}$  events are selected from data using same MLP cut including FV cut as described before. Their distribution is already shown in fig 4.15.
- Then, PDFs in  $N_{pe}^{geonorm}$  for  $^{210}\text{Po}$  (fig 4.16) and other species lying in the energy region of  $^{210}\text{Po}$  are created. The other species include  $^7\text{Be}-\nu$ ,  $pep-\nu$ ,  $\text{CNO}-\nu$ ,  $pp-\nu$ ,  $^{210}\text{Bi}$ , and  $^{85}\text{Kr}$ .
- Further the PDFs of other species are summed together with interaction rate of species as weights, as predicted by HZ-SSM predictions or independent estimations. Those values are listed in Table 4.2.
- The summed PDF is shown in Fig 4.17. It represents  $\beta$  spectrum (in blue) and an exponential damping (in red) is applied to this spectrum to simulate MLP

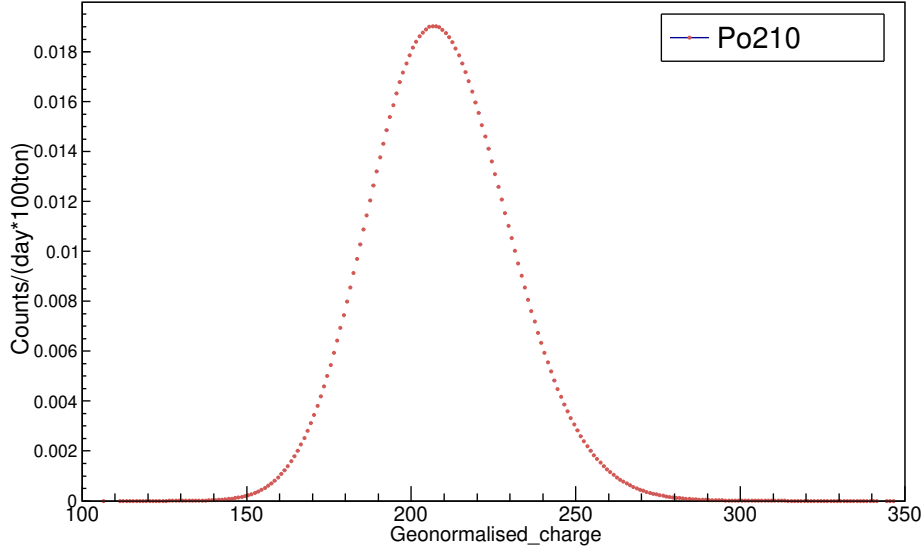


**Figure 4.16:** The figure shows the MC PDF of  $^{210}\text{Po}$ .

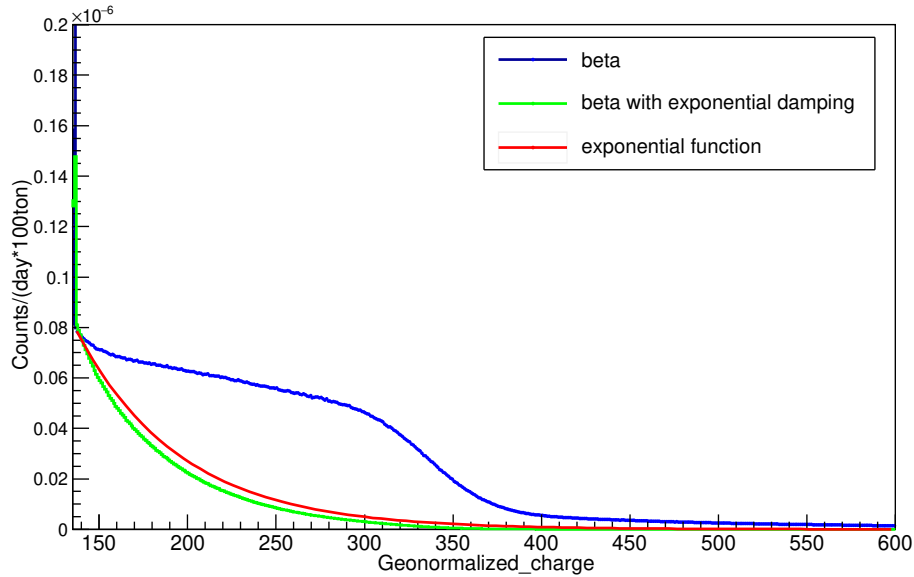


**Figure 4.17:** The figure shows the MC PDF of  $\beta$  events. It represents  $\beta$  spectrum (in blue) and an exponential damping (in red) is applied to this spectrum to simulate MLP dependence of tagging  $\beta$  events as  $\alpha$  events on energy. The resulting PDF is shown in green.

dependence of tagging  $\beta$  events as  $\alpha$  events on energy. The resulting PDF is shown in green.

- At last, the produced PDFs are used to fit  $^{210}\text{Po}$  data. The fit results for best configuration is shown in Fig 4.18. Here, we obtain a good p-value of 0.64 and better residuals than shown in Fig 4.16 which shows the fit results for Gaussian and Exponential fit method.
- From this fit, the rate of  $\beta$  events in energy region ( $150 < N_{pe}^{geonorm} < 270$ ) chosen

Species	Rate of interaction (cpd/100 ton)
${}^7\text{Be}-\nu$	47.9
$pep-\nu$	2.74
CNO- $\nu$	4.92
${}^{210}\text{Bi}$	12.5
$pp-\nu$	131.1
${}^{85}\text{Kr}$	9.8

**Table 4.2:** The value of rate of interaction for different species spanning in the energy region of  ${}^{210}\text{Po}$ .

for analysis of minimum  ${}^{210}\text{Po}$  rate is 2.6 cpd/100 ton.

- To evaluate systematics associated to this method, various parameters like fit range (Fig 4.19 and Fig 4.20) and slope of exponential function (Fig 4.21) which is used to model MLP dependence of tagging  $\beta$  events as  $\alpha$  events on energy is varied. The total systematic uncertainty is calculated to be 0.3 cpd/100 ton.
- Hence, the results of the 2 methods are compatible with each other.

After fitting the monthly  ${}^{210}\text{Po}$  data using equation 44 and aligning the data with respect to  $z_0$ , the final fit is performed over data of whole period using the same equation (44) and obtain a minimum  ${}^{210}\text{Po}$  rate of 11.5 cpd/100 ton. Hence, an upper limit on  ${}^{210}\text{Bi}$  rate in this LPoF region is 11.5 cpd/100 ton with statistical uncertainty of 0.8 cpd/100 ton.

In order to extrapolate  ${}^{210}\text{Bi}$  rate over whole FV, studies regarding its spatial distribution has been made. To do so, the  $\beta$  events were selected in the energy window where contribution of  ${}^{210}\text{Bi}$  is maximum with respect to other species inside FV. The studies have shown that  ${}^{210}\text{Bi}$  is uniform in FV during Phase-3 [28]. The uncertainty in determination of this homogeneity is taken into account as systematic error corresponding to the value of 0.8 cpd/100 ton.

Other systematic errors include mass of the fit region of  ${}^{210}\text{Po}$  data with value of 0.4 cpd/100 ton and bin width of histograms with value of 0.2 cpd/100 ton. Combining all the errors, the final upper limit on  ${}^{210}\text{Bi}$  rate is  $11.5 \pm 1.3$  cpd/100 ton.

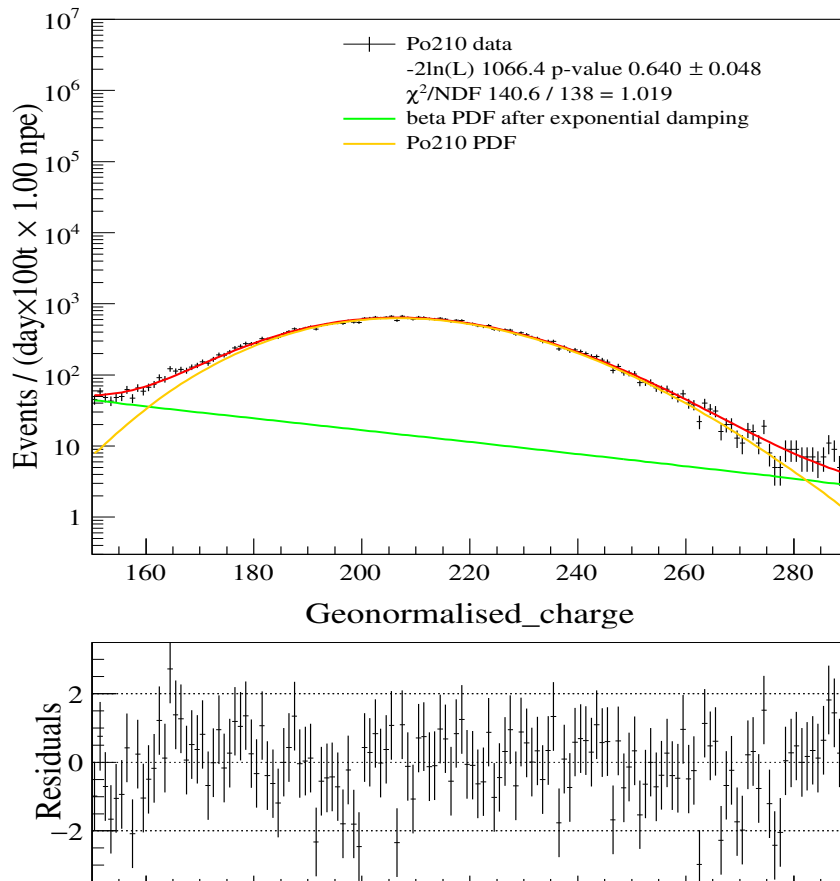


**Figure 4.18:** The figure shows the best fit results of  $^{210}\text{Po}$  data with exponentially damped  $\beta$  PDF (in purple) and  $^{210}\text{Po}$  PDF (in yellow) including residuals. One can see the good p-value of 0.64 and better residuals than shown in Fig 4.16.

Variation of  $\beta$  rate with low fit range

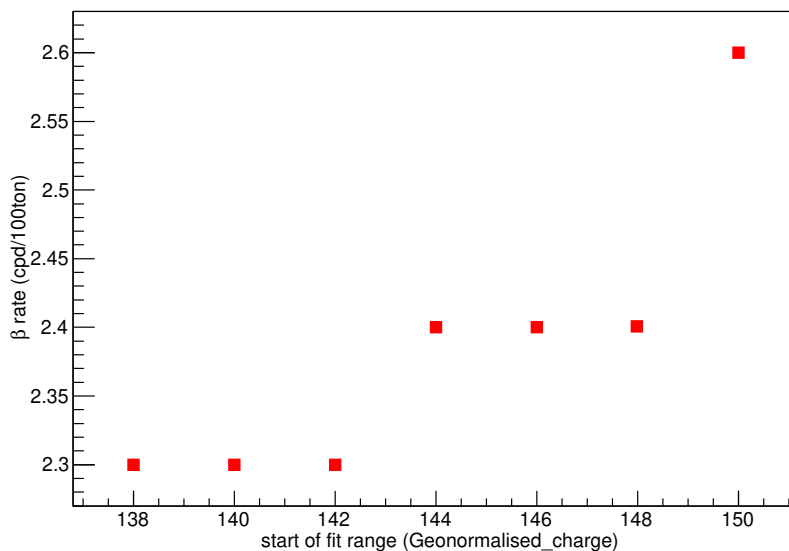


**Figure 4.19:** The figure shows the variation of  $\beta_{leak}$  with respect to lower value of fit range when high value of fit range is fixed to 290.

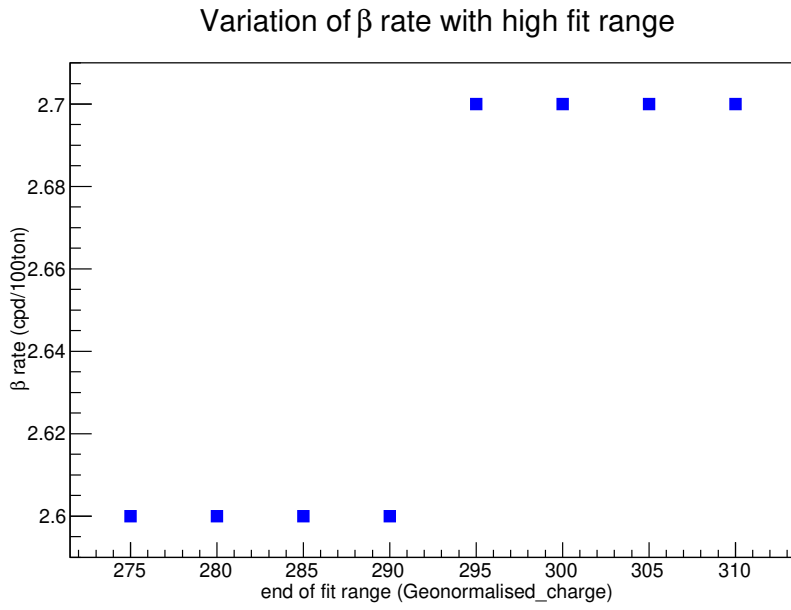


**Figure 4.20:** The figure shows the variation of  $\beta_{leak}$  with respect to higher value of fit range when low value of fit range is fixed to 150.

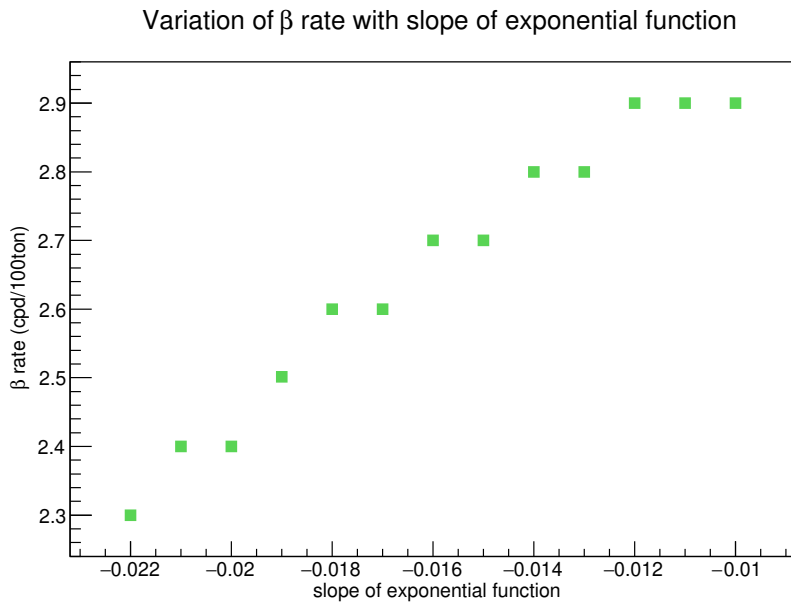


**Figure 4.21:** The figure shows the variation of  $\beta_{leak}$  with respect to slope of exponential function used to simulate the MLP dependence on energy.

## Chapter 5

# Multivariate Monte Carlo Fit of Data

This chapter explains the technique of fitting used to extract the CNO- $\nu$  signal from Phase-3 data in section 5.1. It also explains the technique of applying a constraint as penalty or upper limit on rates of individual spectral component.

The results obtained using the multivariate monte carlo fit of Phase-3 data are quoted in section 5.2. I participated in performing the fit using the framework developed by Borexino Collaboration known as bx-GooStats. This section also mentions about the fit configuration used, and cites the  $1\sigma$  confidence interval obtained for CNO- $\nu$  rate.

### 5.1 Fitting Method

In order to disentangle CNO- $\nu$  signal and background from data, a fitting method is used which exploits the difference in energy and radial distributions of neutrino signal and backgrounds. In order to perform the analysis of Phase 3 data, whose results will be quoted in next section, a technique of multivariate fit of data is adopted.

In this technique, a binned likelihood function containing information from 2 energy spectra - TFC-tagged and TFC-subtracted (described in section 4.1.1) in addition to the information from radial distribution of the events in an optimized energy region, is maximised. The importance of radial distribution lies in the fact that it helps to disentangle the external background contribution from data as it has an exponential trend decreasing until center of the detector. The maximisation is done such that the reference shapes generated through MC simulations i.e MC PDFs (discussed in chapter 3) describes the data well.

The total likelihood function is calculated as the following:

$$\mathcal{L}(\vec{k}|\vec{\theta}) = \mathcal{L}_{\text{sub}}^{\text{TFC}}(\vec{k}|\vec{\theta}) \cdot \mathcal{L}_{\text{tag}}^{\text{TFC}}(\vec{k}|\vec{\theta}) \cdot \mathcal{L}_{\text{Rad}}(\vec{k}|\vec{\theta}). \quad (45)$$

The  $\vec{\theta}$  represents the set of parameters with respect to which likelihood is maximised, which are the interaction rates of species. And,  $\vec{k}$  represents the set of experimental data used to calculate the likelihood. Each likelihood term related to TFC-tagged and TFC-subtracted energy distributions in eq. 45 is calculated as standard Poissonian likelihood as following:

$$\mathcal{L}^{\text{TFC}}(\vec{k}|\vec{\theta}) = \prod_{i=1}^N \frac{\lambda_i(\vec{\theta})^{k_i}}{k_i!} e^{-\lambda_i(\vec{\theta})}, \quad (46)$$

where the product goes over each bin  $i$  of  $N$  bins in spectrum and  $k_i$  are the number of entries of events in  $i$ th bin. The  $\lambda_i$  parameter is the expected number of entries for the bin  $i$ .

The likelihood  $\mathcal{L}_{\text{Rad}}(\vec{k}|\vec{\theta})$  is calculated using scaled Poissonian likelihood as following:

$$\mathcal{L}_{\text{Rad}}(\vec{k}|\vec{\theta}) = \prod_{i=1}^N \frac{a\lambda_i(\vec{\theta})^{k_i}}{k_i!} e^{-a\lambda_i(\vec{\theta})}, \quad (47)$$

where  $a$  is a scaling factor which is calculated using normalization to total number of entries in data histogram as:

$$N_{\text{entries}} = a \sum_{i=1}^N \lambda_i(\vec{\theta}). \quad (48)$$

This normalization is done to take into account the correlation which is introduced due to the presence of same entries in both energy spectra and radial distribution.

In the fitting method, the rate of interaction for all species is left free. However, the rate of interaction for some of the species might be required to be constrained like for  $pep-\nu$  rate and upper limit on  $^{210}\text{Bi}$  rate for CNO- $\nu$  analysis as discussed in chapter 4. If a constraint is applied, a symmetric Gaussian penalty term is added to the likelihood as following:

$$\mathcal{L}(\vec{k}|\vec{\theta}) \rightarrow \mathcal{L}(\vec{k}|\vec{\theta}) \cdot \exp\left(-\frac{(x - \mu)^2}{2\sigma^2}\right), \quad (49)$$

where  $\mu$  and  $\sigma$  represent the value of constraint and its error from independent estimations and  $x$  is the fit value of parameter of interest. In case of an upper limit (like for  $^{210}\text{Bi}$  rate in CNO analysis), an asymmetric half Gaussian term is applied such that the value of parameter of interest is left unconstrained between 0 and the value of upper limit.

## 5.2 Fit Results of Phase 3 Data

After passing the data selection cuts described in section 4.1, the data is fitted using MC PDFs via the multivariate method as explained in previous section. The choice of energy estimator for the fit is  $N_h^{\text{norm}}$  (section 2.4). The start of energy range chosen for fit is  $136 N_h^{\text{norm}}$  ( $\approx 0.32$  MeV) excluding the contribution from  $^{14}\text{C}$  decay and pile-up. This is required because decreasing number of live PMTs in the detector has led to the loss of energy and position resolution impacting the low energy region.

The fit results obtained in the energy range 136 to 954 normalized  $N_h^{\text{norm}}$  are shown in Fig 5.1. A good p-value of 0.3 can be seen from the plots. The fit result for radial distribution is depicted in Fig 5.2, where events lying in 500-900  $N_h^{\text{norm}}$  are selected. Since TFC splits the data on the basis that if an event is cosmogenic or not, there are 2 independent parameters (rate of interaction in TFC-tagged and TFC-subtracted spectra) for cosmogenic events while non-cosmogenic events have 1 parameter which are left free in the fit. As already mentioned, the rate of interaction for different species is left free in the fit with the exception of  $pep-\nu$  and  $^{210}\text{Bi}$  rate. The  $^8\text{B}$  interaction rate is fixed according to HZ-SSM predictions, however this does not affect the low energy species rate. Also,

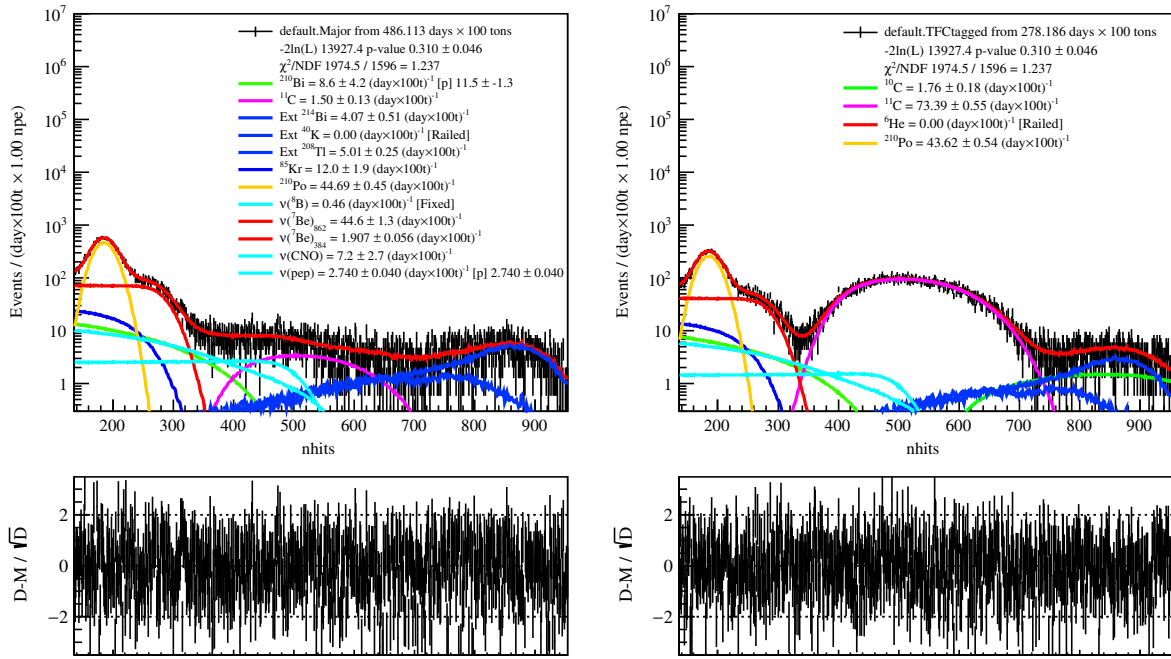


**Figure 5.1:** The figure shows the MV fit results on TFC-subtracted spectra (on the left) and TFC-tagged spectra (on the right) using MC PDFs (in colorful legends) including the distribution of residuals for each spectrum.

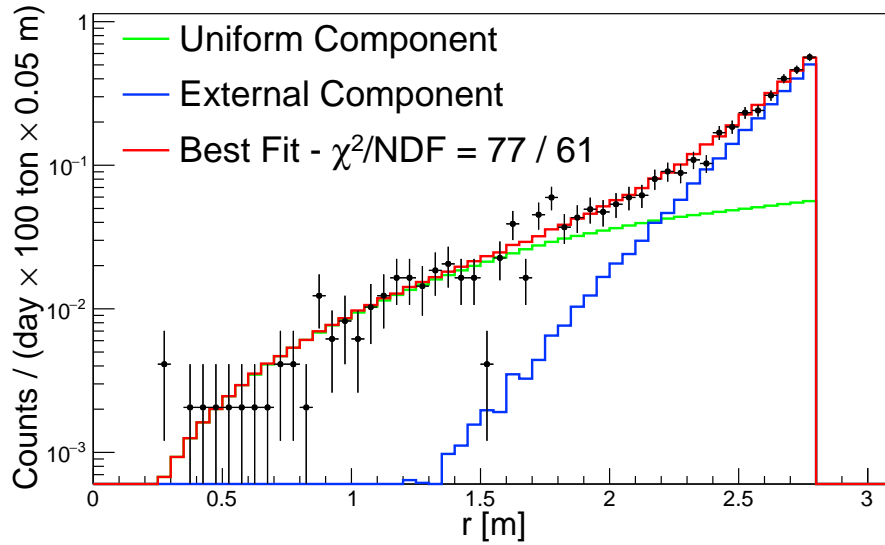


**Figure 5.2:** The figure shows the fit results on the radial distribution of homogeneous internal and external components using respective PDFs produced by MC<sup>1</sup>.

the shifts to the MC PDFs of <sup>11</sup>C (section 4.1.1) and <sup>210</sup>Po are applied.

The results on interaction rate obtained from this MV fit on Phase-3 data with their statistical errors are reported in Table 5.1. From this fitting method, the CNO-ν rate is extracted to be 7.2 cpd/100 ton. From the log likelihood profile of CNO-ν rate shown in Fig 5.3, it can be inferred that the q-value (defined in equation 50) is 30.05 which helps

<sup>1</sup>Source: Borexino Collaboration

to determine the discovery power of CNO- $\nu$  as explained in chapter 6.

$$q = -2\log \frac{\mathcal{L}(\text{CNO} = 0)}{\mathcal{L}(\text{CNO})}, \quad (50)$$

where  $\mathcal{L}(\text{CNO} = 0)$  and  $\mathcal{L}(\text{CNO})$  are the likelihood values for CNO rate = 0 cpd/100t and the value from the fit.

The likelihood profile is asymmetric in shape due to the usage of half Gaussian term as penalty to evaluate upper limit  $^{210}\text{Bi}$  rate as mentioned in previous section. The asymmetric confidence interval on CNO- $\nu$  rate is evaluated to be -1.7 cpd/100 ton and +2.9 cpd/100 ton. This was calculated using conversion of likelihood profile to PDF of CNO- $\nu$  rate according to probability =  $\exp(-\frac{\Delta x^2}{2})$  and taking 68% quantile as  $1\sigma$  confidence interval (C.I).

Species	Rate of interaction (cpd/100 ton)
$^7\text{Be}-\nu$	$46.5 \pm 1.4$
$pep-\nu$	$2.74 \pm 0.04$ (constrained)
CNO- $\nu$	$7.2 -1.7 +2.9$
$^8\text{B}-\nu$	0.46 (fixed)
$^{210}\text{Bi}$	$11.5 \pm 1.3$ (UL)
$^{85}\text{Kr}$	$12.0 \pm 1.9$
External $^{214}\text{Bi}$	$4.07 \pm 0.51$
External $^{208}\text{Tl}$	$5.01 \pm 0.25$
External $^{40}\text{K}$	0.00
$^6\text{He}$	0.00
$^{10}\text{C}$	$1.76 \pm 0.18$
$^{11}\text{C}$ (tagged)	$73.39 \pm 0.55$
$^{11}\text{C}$ (subtracted)	$1.50 \pm 0.13$
$^{210}\text{Po}$ (tagged)	$44.69 \pm 0.45$
$^{210}\text{Po}$ (subtracted)	$43.62 \pm 0.54$

**Table 5.1:** The value of the rate of interaction (with statistical error only) for different species obtained from MV Monte Carlo fit on Phase 3 data.

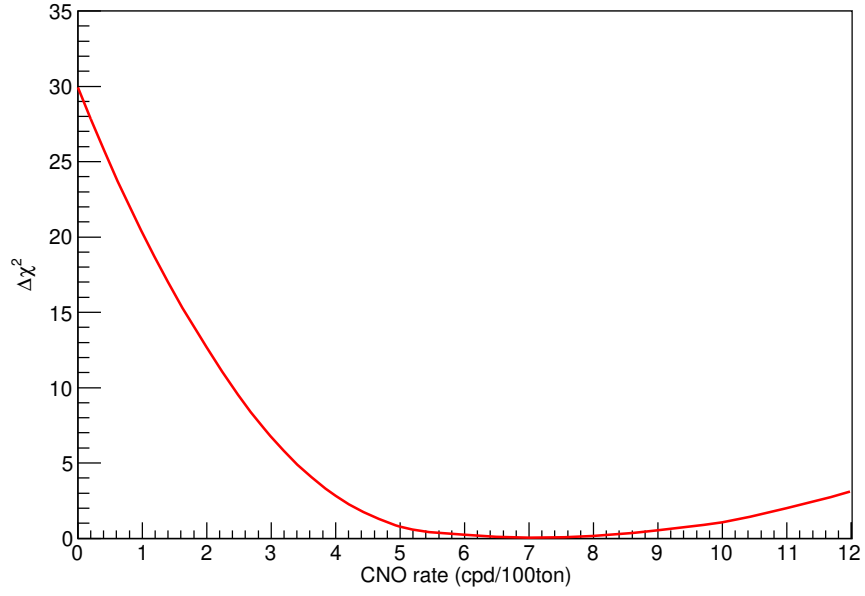


**Figure 5.3:** The figure shows the log likelihood profile for CNO- $\nu$  rate (with statistical error only). Here, CNO- $\nu$  rate of 0 cpd/100 ton corresponds to  $\Delta\chi^2 = -2\Delta\ln\mathcal{L} = 30.05$ .

## Chapter 6

# Final Result with systematics

This chapter describes the studies of systematic effects on CNO- $\nu$  rate and its discovery significance. In section 6.1, the error related to the multivariate Monte Carlo fitting method is also explained.

Section 6.2 consists of list of sources of error originating due to Monte Carlo fit model. My work lies in this section to determine the magnitude of deformation for simulated data-sets accounting for energy scale in detector energy response and  $^{11}\text{C}$  shift. The final results for CNO- $\nu$  rate and significance of rejecting null hypothesis including all the uncertainties are quoted in section 6.3.

### 6.1 Systematics related to Fitting Method

As we saw in chapter 5, the MV fit for CNO- $\nu$  analysis is based on the likelihood that consists of contribution from 3 distributions: TFC-tagged, TFC-subtracted and radial distribution. In order to study the systematics related to this fitting method, the study of CNO- $\nu$  rate was done in different fit configurations.

The parameters that were varied to study systematics include minimum and maximum energy range of the 2 two energy spectra, minimum and maximum energy of events that contribute to the radial distribution and its binning. It accounts for 2500 fits in total and error on CNO- $\nu$  was found to be negligible compared to statistical uncertainty ( $\sim 0.17$  cpd/100 ton). The systematic error on q-value associated to the Multivariate Monte Carlo fitting method has also been evaluated to be negligible.

### 6.2 Other Sources of Systematics

The other sources of systematics are related to the data-sets generated through Monte-Carlo simulations. As PDFs are based on MC simulation, it is important to account for the sources that could affect or bias the CNO- $\nu$  rate or its significance. The sources of systematics influencing the CNO- $\nu$  are listed as following:

- **The Spectral Shape of  $^{210}\text{Bi}$**  - Different measurements has yielded the difference in the shape of electron recoil spectrum at low energies due to  $^{210}\text{Bi}$  decay. This is crucial because MV Monte Carlo fit rely on the reference shapes of each species and also, the shape is taken into account for using the value of constraint on  $^{210}\text{Bi}$  rate. The studies [34] has shown that the maximum deviation from shape chosen for analysis amounts to 18%.

- **The Spectral Shape of  $^{11}\text{C}$**  - The removal of noise events by MLP cuts (chapter 4) in  $^{11}\text{C}$  region cause the deformation in the shape of  $^{11}\text{C}$  simulated spectra. This distortion of PDF has been evaluated to be 2.3%.
- **Energy scale** - The energy scale parameter related to detector energy response agrees to a certain level in data and MC as discussed in section 3.2. This level of precision was taken into account through systematics. In order to understand the precision level, the peak of energy spectra of  $^{210}\text{Po}$  was compared in both data and MC. The method to compare the peak is described in section 3.2. This has resulted in the discrepancy of  $\sim 0.32\%$ .
- **$^{11}\text{C}$  shift** - For  $^{11}\text{C}$ , the method to compare the peak in PDF and data is discussed in section 4.1.1. The uncertainty of shift value of  $0.7 N_{hits}$  ( $\sim 0.1\%$ ) is taken to account for systematics which is calculated using likelihood profile as shown in section 4.1.1.
- **Non-uniformity and Non-linearity** - These effects were studied using data from calibration sources and their Monte Carlo simulations. Inaccuracies accounting for spatial non-uniformity and non-linearity in detector response are 0.28% and 0.4% respectively.

### 6.3 Final Results

In order to evaluate the systematics error on CNO rate, over a million of simulated data-sets were produced using toy Monte Carlo both with distortions which are listed above and also without any deformations injecting different value of CNO- $\nu$  rate. The magnitude of deformations are also mentioned in section 6.2. Further, both data-sets are fitted using standard reference shapes without any deformations. Then, the widths of the distribution of CNO- $\nu$  rate for both configurations are compared and the systematic error on CNO- $\nu$  rate is evaluated to be -0.5 and +0.6 cpd/100ton.

This systematic error is combined with likelihood profile shown in Fig 5.3 by smearing the PDF of CNO- $\nu$  rate with mentioned uncertainty and taking 68% quantile of this smeared PDF as  $1\sigma$  confidence interval. The C.I on CNO- $\nu$  rate including the systematics from the resulting profile is calculated to be -1.7 and +3.0 cpd/100ton (68% confidence level). This is depicted in Fig 6.1. The null hypothesis of no CNO- $\nu$  is rejected at the significance level of  $5.1\sigma$  which is also calculated using the probability distribution. This translates to a CNO- $\nu$  flux of  $7.0_{-2.0}^{+3.0} \times 10^8 \text{ cm}^{-2} \text{ s}^{-1}$  on Earth.

An additional frequentist hypothesis test [36] was made using toy Monte Carlo to evaluate the significance of excluding the CNO- $\nu$  rate of 0 cpd/100 ton. In this test, 13.8 million data-sets were simulated without injected CNO- $\nu$  rate. These data-sets are fitted using distorted PDFs in order to obtain the distribution of q-value. In order to claim the significance of  $5.0\sigma$ , p-value should be less than  $2.8 \times 10^{-7}$  as cited in [36]. One can see from Fig 6.2 that no event has q-value larger than that of obtained from data (chapter 5). This implies that the null hypothesis of no CNO- $\nu$  is rejected with a significance of  $>5.0\sigma$  at 99% confidence level which is compatible with the one obtained from data.

The distribution of q-value is also obtained with injected CNO- $\nu$  rate of 7.2 cpd/100 ton in the same way as described before. One can see from Fig 6.2 that the q-value from data (chapter 5) lies in the expected distribution (shown in red).

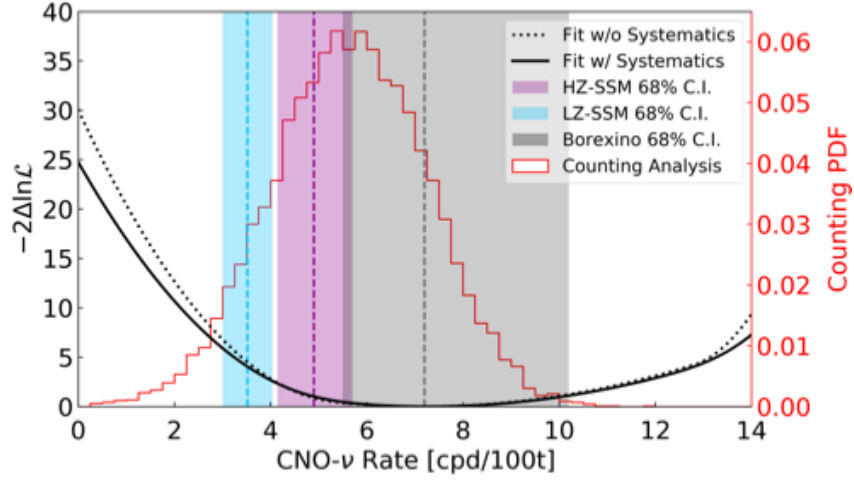


**Figure 6.1:** The figure shows the likelihood profile of CNO- $\nu$  rate without including the systematic errors (dashed line) and with systematic errors (black line). The histogram shows the PDF of CNO-rate (see text) obtained from the counting analysis. The bands in blue, violet and grey represents the confidence interval (68%) for SSM-LZ predictions, SSM-HZ predictions, and the result from Borexino respectively<sup>1</sup>.

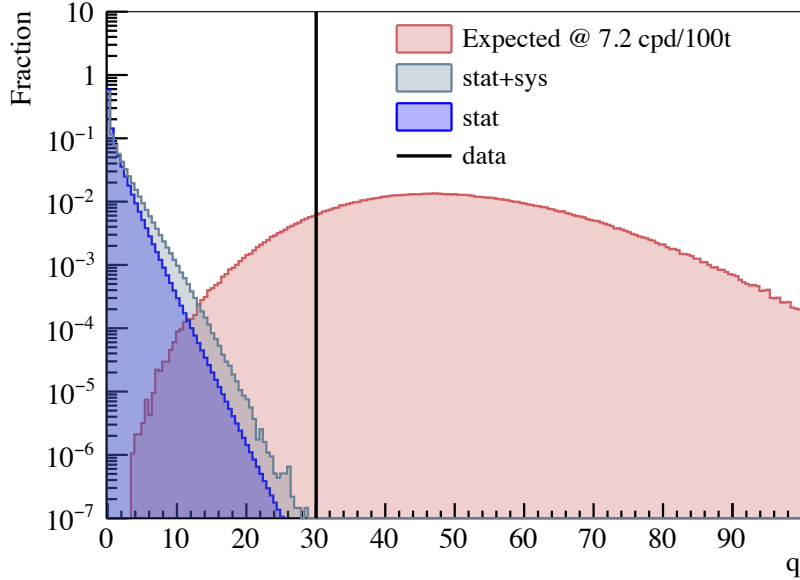


**Figure 6.2:** The figure shows the  $q$ -distribution for simulated pseudo data-sets without any CNO injected including systematics (in grey) and no systematics (in blue). The histogram in red shows expected distribution of  $q$ -value for data-sets injected with CNO- $\nu$  rate of 7.2 cpd/100 ton (the best fit value from data) including the systematic distortions. The black corresponds to the  $q$ -value of 30.05 obtained from data in chapter 5<sup>1</sup>.

## 6.4 Counting Analysis

A simplified method called as "Counting Analysis" [35] has been developed which act as a complementary analysis to the robust method of multivariate Monte Carlo fit. Its strategy is to exploit the region of interest (ROI) where Figure of Merit (which means the expected discovery significance of CNO neutrinos) is maximised. This analysis is performed using

<sup>1</sup>Source: Borexino Collaboration

geonormalised charge ( $N_{pe}^{geonorm}$ ) as energy estimator variable and the results are obtained with analytical response of the detector in energy range of  $180 < N_{pe}^{geonorm} < 1000$ . All the events lying in ROI of  $375 < N_{pe}^{geonorm} < 429$  (780-885 keV) are counted and further, subtract the contribution of events from all the identified background events in that energy region. The same value of constraint on  $pep-\nu$  and  $^{210}\text{Bi}$  rate is applied in this approach as described before. Hence, the rate on CNO- $\nu$  is obtained and the uncertainty is calculated by propagating all errors associated to reference detector response model and independent estimations on background rates. The results for CNO- $\nu$  rate is  $5.6 \pm 1.6$  cpd/100ton at a significance level of  $3.5\sigma$ . This provides the confirmation for the existence of CNO solar neutrinos.

## Chapter 7

# Conclusion and Outlook

As described in this thesis, the goal of the Borexino experiment of detecting CNO solar neutrinos has been achieved. As described before, the contribution to solar energy by CNO fusion cycle is hypothesized to be  $\sim 1\%$  of total solar luminosity while  $pp$ -chain is the major source of energy from the Sun. This poses a challenge in detecting the CNO neutrinos coming from the Sun due to its low rate and presence of backgrounds like  $pep$ - $\nu$  and  $^{210}\text{Bi}$  whose rate is correlated to CNO- $\nu$  rate. This cycle is believed to be a dominant source of energy in stars massive than the Sun.

Due to degenerate spectral shape of  $pep$ - $\nu$ ,  $^{210}\text{Bi}$  and CNO- $\nu$ , it is difficult to disentangle the CNO- $\nu$  signal from data using fitting method without any constraint on correlated species. Hence, the constraints on their rate from independent estimations are applied. The constraint on  $pep$ - $\nu$  rate is based on Standard Solar Model predictions while an upper limit on  $^{210}\text{Bi}$  rate is determined using the link with its daughter  $^{210}\text{Po}$ . The operation of thermal stabilisation of detector in the year 2015 has made an significant contribution to determine upper limit on  $^{210}\text{Bi}$  rate and hence, the the analysis is done only on the Phase-3 data which spans from June 2016 till February 2020.. My work concentrated on determining the values of the parameters of the model used to estimate this upper limit.

The analysis on Phase-3 data has been performed in higher energy range excluding the contribution from  $^{14}\text{C}$  and pile-up events using the fitting method called Multivariate Monte Carlo fitting technique. This method makes an extensive use of simulated datasets using Monte Carlo simulations and I have worked towards its optimisation which has been described in this thesis.

Besides these lists of obstacles, the first experimental detection of CNO- $\nu$  has been made which is a proof for the occurrence of CNO cycle in the Sun. The rejection of non-existence of CNO- $\nu$  has been made with a significance better than  $5.0\sigma$  at 99.0% confidence level. Taking into account all the statistical and systematic uncertainties, the estimation of CNO- $\nu$  rate is  $7.2_{-1.7}^{+3.0}$  cpd/100ton which corresponds to a flux of  $7.0_{-2.0}^{+3.0} \times 10^8 \text{ cm}^{-2} \text{ s}^{-1}$ . The existence of CNO- $\nu$  has also been confirmed using a simplified cross-check method called counting analysis.

However, this measured rate of CNO- $\nu$  has been found compatible with both SSM-HZ and SSM-LZ predictions. The HZ and LZ SSM hypothesis is disfavoured at the significance of  $1.2\sigma$  and  $2.1\sigma$  respectively. Hence, the current measurement can not solve the solar metallicity problem.

As the Borexino detector continues data-taking further, the analysis towards the precise measurement of CNO- $\nu$  flux will continue to decrease the uncertainties associated to it. If clean LPoF enlarges throughout the whole fiducial volume, this could reduce the uncertainty on the determination of upper limit on  $^{210}\text{Bi}$  rate or even the true measurement of  $^{210}\text{Bi}$  rate. There will be an effort to do the analysis without using the constraint on  $^{210}\text{Bi}$  rate. This has been proposed to perform spectral analysis around the  $^{210}\text{Bi}$  end-point region where the difference in energy spectra of  $^{210}\text{Bi}$  and CNO- $\nu$  can be exploited using larger data exposure (from both Phase-2 and Phase-3) and also using the *pep- $\nu$*  constraint.

Further, the analysis work regarding the directionality measurement of solar neutrinos using Cherenkov light emission due to interaction of neutrinos in Borexino detector will be carried out and use it in the measurement of CNO- $\nu$ . The preliminary studies shows that the directionality of  $^7\text{Be}$  solar neutrinos using Cherenkov light emission has been measured. These developments in the methods could provide the robust studies on CNO cycle and the insight in understanding the metallicity hypothesis of Standard Solar Models, currently to which there is no sensitivity.

## Chapter 8

# Publications

- M. Agostini, K. Altenmüller, S. Appel, V. Atroshchenko, Z. Bagdasarian, D. Basilico, G. Bellini, J. Benziger, R. Biondi, D. Bravo, B. Caccianiga, F. Calaprice, A. Caminata, P. Cavalcante, A. Chepurinov, D. D'Angelo, S. Davini, A. Derbin, A. Di Giacinto, V. Di Marcello, X.F. Ding, A. Di Ludovico, L. Di Noto, I. Drachnev, A. Formozov, D. Franco, C. Galbiati, C. Ghiano, M. Giammarchi, A. Goretti, A.S. Göttel, M. Gromov, D. Guffanti, Aldo Ianni, Andrea Ianni, A. Jany, D. Jeschke, V. Kobychyev, G. Korga, S. Kumaran, M. Laubenstein, E. Litvinovich, P. Lombardi, I. Lomskaya, L. Ludhova, G. Lukyanchenko, L. Lukyanchenko, I. Machulin, J. Martyn, E. Meroni, M. Meyer, L. Miramonti, M. Misiaszek, V. Muratova, B. Neumair, M. Nieslony, R. Nugmanov, L. Oberauer, V. Orekhov, F. Ortica, M. Pallavicini, L. Papp, L. Pellicci, Ö. Penek, L. Pietrofaccia, N. Pilipenko, A. Pocar, G. Raikov, M.T. Ranalli, G. Ranucci, A. Razeto, A. Re, M. Redchuk, A. Romani, N. Rossi, S. Schönert, D. Semenov, G. Settanta, M. Skorokhvatov, A. Singhal, O. Smirnov, A. Sotnikov, Y. Suvorov, R. Tartaglia, G. Testera, J. Thurn, E. Unzhakov, F.L. Villante, A. Vishneva, R.B. Vogelaar, F. von Feilitzsch, M. Wojcik, M. Wurm, S. Zavatarelli, K. Zuber, G. Zuzel., "First Direct Experimental Evidence of CNO neutrinos", The BOREXINO Collaboration, arXiv:2006.15115v1, June 2020.

# Bibliography

- [1] <https://journals.aps.org/pr/pdf/10.1103/PhysRev.55.434>
- [2] <https://www.nobelprize.org/prizes/themes/how-the-sun-shines-2/>
- [3] The Astrophysical Journal 687 (2008) 678 doi:10.1086/591787
- [4] C. F. von Weizsäcker, “Über Elementumwandlungen in Innern der Sterne. II,” *Physikalische Zeitschrift*, 39, 633 (1938)
- [5] <http://www.sns.ias.edu/jnb/>
- [6] Núria Vinyoles et al. “A new Generation of Standard Solar Models”. In: *Astrophys. J.* 835.2 (2017), <https://iopscience.iop.org/article/10.3847/1538-4357/835/2/202/pdf>
- [7] B. T. Cleveland et al. “Measurement of the solar electron neutrino flux with the Homestake chlorine detector”. In: *Astrophys. J.* 496 (1998).
- [8] [https://doi.org/10.1016/S0168-9002\(03\)00425-X](https://doi.org/10.1016/S0168-9002(03)00425-X)
- [9] Hosaka J et al. 2006 *Phys. Rev. D* 73 112001
- [10] Anselmann P et al. (GALLEX Collaboration) 1992 *Phys. Lett. B* 285 390
- [11] Anselmann P et al. (GALLEX Collaboration) 1995 *Phys. Lett. B* 342 440
- [12] Altmann M et al. 2005 *Phys. Lett. B* 616 214
- [13] Measurement of the solar neutrino capture rate with gallium metal. III. Results for the 2002–2007 data-taking period, J. N. Abdurashitov et al (SAGE Collaboration), *Phys. Rev. C* 80, 015807
- [14] Direct Evidence for Neutrino Flavor Transformation from Neutral-Current Interactions in the Sudbury Neutrino Observatory, *Phys Rev. Lett* 89
- [15] Q. R. Ahmad et al., *Phys. Rev. Lett.* 87 , 071301 (2001).
- [16] The Sudbury Neutrino Observatory, Nick Jelley, Arthur B. McDonald and R.G. Hamish Robertson, *Annu. Rev. Nucl. Part. Sci.* 2009, doi : 10.1146/annurev.nucl.55.090704.151550
- [17] G. Alimonti et al. “The Borexino detector at the Laboratori Nazionali del Gran Sasso”. In: *Nucl. Instrum. Meth. A* 600 (2009)
- [18] G. Bellini et al. (Borexino Collaboration): "Final results of Borexino Phase-I on low-energy solar-neutrino spectroscopy", *Phys. Rev. D*, 89:112007, Jun 2014.
- [19] M. Agostini et al. (Borexino Collaboration), "Simultaneous Precision Spectroscopy of pp,  $^7\text{Be}$ , and pep Solar Neutrinos with Borexino Phase-II", arXiv:1707.09279. *Physical Review D* 100 (2019) p. 082004

- [20] "Echidna Documentation", Internal document on Borexino Document Database.
- [21] M. Agostini et al. (Borexino Collaboration): "Seasonal modulation of the  $7\text{Be}$  solar neutrino rate in Borexino", *Astroparticle Physics*, Volume 92 (2017)
- [22] L. Ludhova. Low energy neutrino physics lectures - solar neutrinos, Institute III B, Faculty of Mathematics, Computer Science and Natural Sciences, RWTH Aachen University, Summer Semester 2020.
- [23] M. Agostini et al. "The Monte Carlo simulation of the Borexino detector". In: *Astropart. Phys.* 97 (2018)
- [24] H. Back et al. "Borexino calibrations: hardware, methods, and results", *Journal of Instrumentation*, 7(10):P10018, 2012.
- [25] J. Bergström, M.C. Gonzalez-Garcia, M. Maltoni, C. Peña-Garay, A.M. Serenelli, and N. Song. *JHEP*, 2016:132, 2016.
- [26] Luminosity constraint and entangled solar neutrino signals, <https://arxiv.org/pdf/1808.01495.pdf>
- [27] N. Rossi, M. Agostini, P. Cavalcante, X. Ding, D. Guffanti, A. Ianni, M. Misiaszek, and F. Calaprice, "Feasibility study of the link between  $210\text{Bi}$  and  $210\text{Po}$  in the Borexino PhaseII." Internal document, Nov 2017.
- [28] D. Basilico, "First indication of solar neutrinos from the CNO cycle reactions with the Borexino experiment". PhD thesis, University of Milan, 2020-02-07.
- [29] Alexandre Göttel and Sindhuja Kumaran, "A Bayesian framework for the  $210\text{Po}$  "clean region" analysis in the search of CNO", An Internal document on Borexino Document Database.
- [30] S. Kumaran, "Extraction of  $210\text{Bi}$  via  $210\text{Po}$  for CNO neutrino detection with Borexino", Poster in Neutrino Conference 2020.
- [31] M. Redchuk, "Looking inside the Sun with the Borexino experiment: detection of solar neutrinos from the proton-proton chain and the CNO cycle", PhD thesis, RWTH Aachen University, 2020-08-31.
- [32] M. Gromov, "MLP efficiency", An Internal document on Borexino Document Database.
- [33] O. Smirnov, A. Vishneva, M. Gromov, "Strategy of the alpha/beta discrimination for the joint analysis of the phases 1 and 2", An Internal document on Borexino Document Database.
- [34] F. Calaprice, X. Ding, A. Ianni, and N. Rossi, "Systematics to CNO neutrino evidence from the  $210\text{Bi}$  shape." Internal document on Borexino Document Database.
- [35] R. Biondi, "Counting analysis of Borexino Phase-III data for the detection of CNO solar neutrinos", Poster in Neutrino Conference 2020.
- [36] G. Cowan, K. Cranmer, E. Gross, and O. Vitells, "Asymptotic formulae for likelihood-based tests of new physics," *Eur. Phys. J.*, vol. C71, p. 1554, 2011. [Erratum: *Eur. Phys. J.*C73,2501(2013)]

# Acknowledgements

First of all, I would like to thank my supervisor Prof. Dr. Livia Ludhova for introducing me to the exciting field of neutrino physics through both the course and the research project. She has motivated me and provided me with her valuable support and guidance throughout this project. I am grateful to Dr. Zara Bagdasarian, for supervising me in the initial days of joining of this project when I needed guidance the most. Despite the situation due to Covid-19, it has been fun working with my groupmates, Giulio, Oemer, Mariia, Alex and Sindhu. From meeting online to chilling in park, I have shared good times with them even in this difficult situation. I would also like to thank colleagues in bx-analysis group of Borexino Collaboration for their help throughout. I want to say thanks to my previous supervisors in RWTH Aachen University for giving me opportunity to get some learning experience by working in a research team for the first time. I don't think that the word of thanks is enough for expressing gratefulness to my parents, Rajesh and Beenu Singhal, for all the struggles they have made for me so that I can get the best education possible and for always trusting me. And my siblings, Divyanshi and Aviral, has also been constant source of support. I would be missing a lot if I do not thank my friends in Aachen, Kavita di, Nikita and Ashish, for providing me constant mental support and being my family away from home. And at last, I can never forget to thank my group in bachelors, especially to Shantanu, Kavita, Anju, and Aashri, for always inspiring me to reach where I am today.